

PROBING THE DAWN OF GALAXIES AT $z \sim 9$ –12: NEW CONSTRAINTS FROM HUDF12/XDF AND CANDELS DATA*

P. A. OESCH^{1,7}, R. J. BOUWENS², G. D. ILLINGWORTH¹, I. LABBÉ², M. FRANX², P. G. VAN DOKKUM³, M. TRENTI⁴,
 M. STIAVELLI⁵, V. GONZALEZ⁶, AND D. MAGEE¹

¹ UCO/Lick Observatory, University of California, Santa Cruz, 1156 High Street, Santa Cruz, CA 95064, USA; poesch@ucolick.org

² Leiden Observatory, Leiden University, NL-2300 RA Leiden, The Netherlands

³ Department of Astronomy, Yale University, New Haven, CT 06520, USA

⁴ Institute of Astronomy, University of Cambridge, Madingley Road, Cambridge CB3 0HA, UK

⁵ Space Telescope Science Institute, 3700 San Martin Drive, Baltimore, MD 21218, USA

⁶ University of California, Riverside, 900 University Avenue, Riverside, CA 92507, USA

Received 2013 January 28; accepted 2013 June 20; published 2013 July 26

ABSTRACT

We present a comprehensive analysis of $z > 8$ galaxies based on ultra-deep WFC3/IR data. We exploit all the WFC3/IR imaging over the Hubble Ultra-Deep Field from the HUDF09 and the new HUDF12 program, in addition to the HUDF09 parallel field data, as well as wider area imaging over GOODS-South. Galaxies are selected based on the Lyman break technique in three samples centered around $z \sim 9$, $z \sim 10$, and $z \sim 11$, with seven $z \sim 9$ galaxy candidates, and one each at $z \sim 10$ and $z \sim 11$. We confirm a new $z \sim 10$ candidate (with $z = 9.8 \pm 0.6$) that was not convincingly identified in our first $z \sim 10$ sample. Using these candidates, we perform one of the first estimates of the $z \sim 9$ UV luminosity function (LF) and improve our previous constraints at $z \sim 10$. Extrapolating the lower redshift UV LF evolution should have revealed 17 $z \sim 9$ and 9 $z \sim 10$ sources, i.e., a factor $\sim 3\times$ and $9\times$ larger than observed. The inferred star formation rate density (SFRD) in galaxies above $0.7 M_{\odot} \text{ yr}^{-1}$ decreases by 0.6 ± 0.2 dex from $z \sim 8$ to $z \sim 9$, in excellent agreement with previous estimates. From a combination of all current measurements, we find a best estimate of a factor $10\times$ decrease in the SFRD from $z \sim 8$ to $z \sim 10$, following $(1+z)^{-11.4 \pm 3.1}$. Our measurements thus confirm our previous finding of an accelerated evolution beyond $z \sim 8$, and signify a very rapid build-up of galaxies with $M_{\text{UV}} < -17.7$ mag within only ~ 200 Myr from $z \sim 10$ to $z \sim 8$, in the heart of cosmic reionization.

Key words: galaxies: evolution – galaxies: high-redshift – galaxies: luminosity function, mass function

Online-only material: color figures

1. INTRODUCTION

The launch of the WFC3/IR camera in 2009 signified a major milestone in our ability to observe galaxies within the cosmic reionization epoch at $z \gtrsim 6$. Thanks to its ~ 40 times higher efficiency for detecting galaxies in the near-infrared (NIR) compared to previous cameras on the *Hubble Space Telescope* (*HST*), we have pushed the observational frontier to within only ~ 450 Myr from the big bang. In its first year of operation WFC3/IR resulted in the detection of ~ 130 new galaxies at $z > 6$ (see, e.g., Bouwens et al. 2011b). Three years of science operations of WFC3/IR and several deep extra-galactic surveys have now resulted in a large sample of more than 200 galaxies in the reionization epoch, primarily at $z \sim 7$ and $z \sim 8$ (e.g., Bouwens et al. 2011b; Oesch et al. 2012b; McLure et al. 2013; Schenker et al. 2012; Lorenzoni et al. 2013; Bradley et al. 2012; Yan et al. 2011; Finkelstein et al. 2012; Grazian et al. 2012).

From these samples it has become clear that the build-up of galaxies during the first Gyr was a gradual process at $z < 8$. The end of cosmic reionization at $z \sim 6$ did not noticeably impact the UV LF evolution (at least down to the current limits of $M_{\text{UV}} \simeq -18$ —corresponding to a star formation rate of $\text{SFR} \simeq 1 M_{\odot} \text{ yr}^{-1}$). The build-up of the UV luminosity function (LF) progresses smoothly across the $z \sim 6$ reionization boundary, following a constant trend all the way from $z \sim 8$

to $z \sim 4$. Galaxies typically become brighter by $\sim 30\%$ – 40% per unit redshift accompanied by a proportional (but somewhat larger) increase in the average star formation rate of galaxies (see, e.g., Smit et al. 2012; Papovich et al. 2011).

Given the large samples of galaxies discovered at $z \sim 7$ – 8 , the current observational frontier is at $z \sim 9$ and at earlier times. This is a period when significant evolution of the galaxy UV LF is expected from models (e.g., Trenti et al. 2010; Lacey et al. 2011; Finlator et al. 2011). The observational evidence has been suggestive of a significant drop in the UV luminosity density (LD) at $z > 8$, but has not been conclusive (Bouwens et al. 2011a; Oesch et al. 2012a). As a result, the extent to which the LF and the star formation rate density (SFRD) are evolving at $z > 8$ has been the subject of some debate (see, e.g., Coe et al. 2013; Zheng et al. 2012).

At these early epochs, current galaxy samples are still very small as *HST* is approaching its limits. Initially, only one $z \sim 10$ galaxy candidate was identified (UDFj-39546284), even in extremely deep WFC3/IR imaging of the Hubble Ultra-Deep Field (HUDF) as part of the HUDF09 survey (Bouwens et al. 2011a). When combined with all the existing data over the Chandra Deep Field South (CDFS), this one source suggested that the galaxy population is changing quickly, building up very rapidly from $z \sim 10$ to $z \sim 8$. In galaxies with $\text{SFR} > 1 M_{\odot} \text{ yr}^{-1}$ (equivalent to $M_{\text{UV}} \simeq -18$ mag), the inferred UV LD was found to increase by more than an order of magnitude in only ~ 200 Myr from $z \sim 10$ to $z \sim 8$ (Oesch et al. 2012a). This is a factor ~ 5 times larger than what would have been expected

* Based on data obtained with the *Hubble Space Telescope* operated by AURA, Inc., for NASA under contract NAS5-26555.

⁷ Hubble Fellow.

from a simple extrapolation of the lower redshift trends of the UV LF evolution to $z \sim 10$.

Several datasets have allowed us to improve these first constraints. The multi-cycle treasury program CLASH (PI: Postman) has provided four sources at $z \gtrsim 9$ (Zheng et al. 2012; Coe et al. 2013; Bouwens et al. 2012a). In particular, the detections of three $z \sim 9$ galaxies around CLASH clusters by Bouwens et al. (2012a) have provided a valuable estimate of the LD in this key redshift range. Estimating volume densities from highly magnified sources found behind strong lensing clusters is challenging, involving systematic uncertainties due to the lensing model. Bouwens et al. (2012a) used a novel technique of comparing the $z \sim 9$ source counts to those at $z \sim 8$ in the same clusters and obtained a good relative LD estimate. Since the $z \sim 8$ density is well established from the field (e.g., Oesch et al. 2012b; Bradley et al. 2012), this gave a more robust measure than trying to infer source densities directly using lensing models. Interestingly, the three $z \sim 9$ candidates from Bouwens et al. (2012a) are completely consistent with the observed drop in the UV LD and an accelerated evolution of the galaxy population that was previously seen at $z > 8.5$ in the HUDF and CDFS by Oesch et al. (2012a).

Two other high-redshift sources detected in the CLASH dataset (one of which is in common with and proceeded the sample of Bouwens et al. 2012a) have added to the available constraints. Coe et al. (2013) and Zheng et al. (2012) discovered two highly magnified $z \sim 10$ ($z \sim 9.6$ and $z \sim 10.7$) galaxies in the analysis of the CLASH cluster data. The LDs inferred from these galaxies are somewhat higher, but are very uncertain. The large errors on the LD from these two detections encompass a wide range of possible trends from $z \sim 8$ to earlier times. However, as we show later in this paper, taken together, the sources from the CLASH dataset along with the latest sources and constraints from the HUDF/CDFS region are consistent with our earlier estimates of substantial accelerated change in the LD from $z \sim 10$ to $z \sim 8$.

Additional progress in exploring the galaxy population at $z > 8$ has been made through gamma-ray burst (GRB) afterglow observations. The current record holder of an independently confirmed redshift measurement was achieved at $z \sim 8.2$ for GRB090423 (Tanvir et al. 2009; Salvaterra et al. 2009), and GRB redshifts were photometrically measured out to $z = 9.4$ (Cucchiara et al. 2011). These measurements can provide additional constraints on the total SFRD in the very early universe, since GRB rates are thought to be an unbiased tracer of the total SFRD (e.g., Kistler et al. 2009; Trenti et al. 2012; Robertson & Ellis 2012).

While the initial results are encouraging, it is clear that our understanding of the galaxy population at $z > 8$ is still far from complete. Given the very small number of sources in each study, it is perhaps not surprising that the UV LD measurements at $z > 8$ are currently all within 1σ – 2σ of each other. A next step forward in exploring the $z \gtrsim 9$ universe can now be taken thanks to the 128 orbit HUDF12 campaign (PI: Ellis, GO12498). While the critical H_{160} observations to discover $z \sim 10$ galaxies only reach deeper by ~ 0.2 mag compared to the previous HUDF09 image, the HUDF12 survey adds deep F140W (JH_{140}) imaging. This allows for Lyman break galaxy (LBG) sample selections at $z \sim 9$ and $z \sim 11$ – 12 (see also Zheng et al. 2012; Bouwens et al. 2012a; Coe et al. 2013).

In a first analysis of their proprietary HUDF12 data, Ellis et al. (2013) compiled a sample of six extremely faint $z \sim 8.6$ – 9.5 galaxy candidates based on a photometric redshift technique.

One of these sources was already in an earlier $z \sim 7.2$ – 8.8 sample of Bouwens et al. (2011b) based on the HUDF09 data set. Ellis et al. (2013) also re-analyzed our previously detected $z \sim 10$ candidate UDFJ-39546284 (Bouwens et al. 2011a; Oesch et al. 2012a). From the three years of WFC3/IR H_{160} data, it is completely clear now that UDFJ-39546284 is a real source as it is significantly detected in all three major sets of data taken in 2009, 2010, and 2012 (Bouwens et al. 2012d). Very surprisingly, however, UDFJ-39546284 appears not to be detected in the new F140W image, indicating that this source either is a very extreme emission line galaxy at $z \sim 2$ or lies at $z \sim 12$ with the spectral break of the galaxy at $\sim 1.6 \mu\text{m}$ (see also Brammer et al. 2013).

With all the HUDF12 data publicly available, we can now extend our search for $z \gtrsim 9$ galaxies to even deeper limits and to higher redshifts than previously possible. In this paper, we perform a search for $z \sim 9$ – 11 galaxies over the HUDF based on the Lyman break technique. This makes use of the fact that the hydrogen gas in the universe is essentially neutral at $z > 6$, which results in near-complete absorption of rest-frame UV photons shortward of the redshifted Ly α line. Star-forming galaxies at $z > 6$ can therefore be selected as blue continuum sources which effectively disappear in shorter wavelength filters. In Section 3.1 we outline our reasons to use a Lyman break selection instead of photometric redshift selection, as is frequently adopted to identify very high redshift galaxies in the literature, e.g., in Ellis et al. (2013).

This paper is an extension of our previous work on a $z \sim 10$ LBG search, making use of the addition of the HUDF12 dataset as well as of the completed CANDELS GOODS-South data, which allows us to derive more stringent limits on the UV LF evolution at $z > 8$. Additionally, we perform a $z \sim 9$ and $z \sim 11$ LBG search using the HUDF12 data and thus provide an alternative analysis to Ellis et al. (2013), who used the HUDF12 data alone to identify $z > 8.5$ galaxy candidates with a photometric redshift selection.

This paper is organized as follows: we start by describing the data used for this study in Section 2 and define our source selection criteria in Section 3, where we also present our $z \gtrsim 9$ galaxy candidates. These are subsequently used to constrain the evolution of the UV luminous galaxy population out to $z \sim 11$ in Section 4, where we present our results. In Section 5, we summarize and discuss further possible progress in this field before the advent of the *James Webb Space Telescope*.

Throughout this paper, we will refer to the *HST* filters F435W, F606W, F775W, F850LP, F098M, F105W, F125W, F140W, F160W as B_{435} , V_{606} , i_{775} , z_{850} , Y_{098} , Y_{105} , J_{125} , JH_{140} , H_{160} , respectively. We adopt $\Omega_M = 0.3$, $\Omega_\Lambda = 0.7$, $H_0 = 70 \text{ km s}^{-1} \text{ Mpc}^{-1}$, i.e., $h = 0.7$. Magnitudes are given in the AB system (Oke & Gunn 1983).

2. THE DATA

The core dataset of this paper is the combination of ultra-deep Advanced Camera for Surveys (ACS) and WFC3/IR imaging over the HUDF09/HUDF12/XDF field. We enhance this deep dataset by using WFC3/IR and ACS data over both HUDF09 parallel fields, as well as all CANDELS and Early Release Science (ERS) data over the GOODS-South field (see Figure 1). These datasets provide valuable constraints on the more luminous sources, particularly by providing limits over a larger area than is covered by the small HUDF09/HUDF12 field. All these datasets include J_{125} and H_{160} imaging in addition

Table 1
The 5σ Depths^a of the Observational Data Used in This Analysis

Field	Area (arcmin ²)	B_{435}	V_{606}	i_{775}	I_{814}	z_{850}	Y_{105}	J_{125}	JH_{140}	H_{160}
HUDF12/XDF ^{b,c}	4.7	29.8	30.3	30.4	29.1	29.4	29.7	29.7	29.7 ^d	29.8
HUDF09-1	4.7	...	29.5	29.3	...	29.3	29.0	29.2	...	29.0
HUDF09-2	4.7	29.5	29.9	29.5	...	29.2	29.0	29.2	...	29.3
ERS	41.3	28.4	28.7	28.2	28.5	28.0	27.8 ^e	28.2	...	28.0
GOODSS-Deep ^b	63.1	28.4	28.7	28.2	29.0	28.1	28.3	28.5	...	28.3
GOODSS-Wide	41.9	28.4	28.7	28.2	28.5	28.0	27.5	27.7	...	27.5

Notes.

^a Measured in circular apertures of $0''.25$ radius.

^b Improved data relative to Oesch et al. (2012a) for $z \sim 10$ galaxy search.

^c An improved reduction of the optical data is used here (the XDF data set; Illingworth et al. 2013) compared to Beckwith et al. (2006), which results in an improvement in depth of ~ 0.1 – 0.2 mag. These reductions are publicly available at: <http://archive.stsci.edu/prepds/xdff/>.

^d Only the HUDF12/XDF field includes deep JH_{140} imaging, which we require for $z \sim 11$ searches and which significantly improves $z \sim 9$ searches.

^e The ERS field was imaged with Y_{098} rather than with Y_{105} .

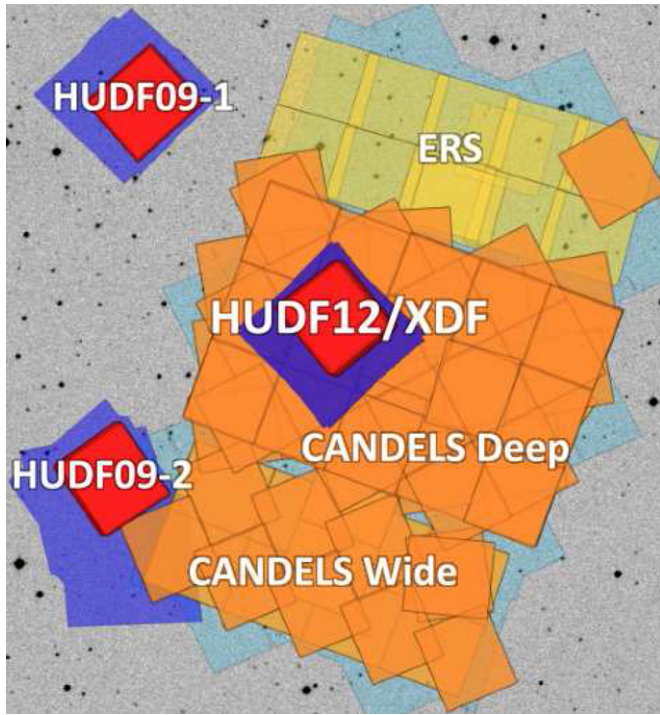


Figure 1. The WFC3/IR fields over the GOODS-South area used in this analysis. The HUDF12/XDF field (dark red) contains the deepest optical and NIR data to date, which reach to ~ 30 AB mag in several bands. The parallel fields HUDF09-1 and HUDF09-2 (also dark red) are only 0.5 – 0.8 mag shallower. The wider area data covering the whole GOODS-S field are from the ERS (yellow) and the CANDELS programs (orange). All these fields include imaging in Y_{105} (or Y_{098} over the ERS), as well as J_{125} and H_{160} , which makes it possible to search for $z \sim 10$ galaxies. The HUDF12/XDF field is additionally covered by very deep JH_{140} imaging, which we exploit to select $z \sim 9$ Lyman break galaxies and obtain some of the first limits on the galaxy population at $z \sim 11$. (A color version of this figure is available in the online journal.)

to deep, multi-band optical ACS data, which allows for reliable $z \sim 10$ galaxy selections (see Section 3.3).

All the WFC3/IR and ACS data are reduced following standard procedures. We subtract a super median image to improve the image flatness and we register to the GOODS ACS frames. For WFC3/IR data we mask pixels affected by persistence using the maps provided by STScI. The ACS data are corrected for charge transfer losses when necessary using

the public code provided by STScI. All images are drizzled to a final pixel scale of $0''.06$, and the rms maps are rescaled to match the actual flux fluctuations in circular apertures of $0''.35$ diameter, dropped down on empty sky positions in the images. The spatial resolution of the data is $\sim 0''.09$ and $\sim 0''.16$ for the ACS and WFC3/IR data, respectively.

The individual datasets used for our analysis are described in more detail in the following sections. They are furthermore summarized in Table 1 and are shown in Figure 1.

2.1. HUDF12/XDF Data

The HUDF (Beckwith et al. 2006) was imaged with WFC3/IR as part of two large *HST* programs now. The HUDF09 (PI: Illingworth; Bouwens et al. 2011b) provided one pointing (4.7 arcmin²) of deep imaging in the three filters Y_{105} (24 orbits), J_{125} (34 orbits), and H_{160} (53 orbits). These data were extended recently with the HUDF12 campaign (Ellis et al. 2013; Koekemoer et al. 2012), which imaged the HUDF further in Y_{105} (72 orbits) and H_{160} (26 orbits), and additionally added a deep exposure in JH_{140} (30 orbits). These are the deepest NIR images ever taken, resulting in a final 5σ depth of $H_{160} \sim 29.8$ mag (see also Table 1).

Since the acquisition of the original optical HUDF ACS data, several programs have added deeper ACS coverage to this region, mainly as part of parallel imaging. We combined all the available ACS data over the HUDF, which allows us to improve the backgrounds and also to push photometry limits deeper by ~ 0.1 – 0.2 mag. These data, along with the matched WFC3/IR data from all programs, are released publicly as the eXtreme Deep Field (XDF) dataset⁸ and are discussed in more detail in Illingworth et al. (2013).

For longer wavelength constraints we also include the ultra-deep *Spitzer*/IRAC data from the 262 hr IUDF program (PI: Labbé; see also Labbé et al. 2012), which reach to ~ 27 mag AB (5σ total) in both [3.6] and [4.5] channels. These data are extremely important for eliminating lower-redshift contaminating sources, particularly intermediate-redshift dusty and/or evolved galaxies (see Section 3.5.1).

⁸ The XDF dataset can be retrieved from MAST at <http://archive.stsci.edu/prepds/xdff/>. For more information see also <http://xdff.uchicago.edu/>.

2.2. HUDF09 Parallel Fields and GOODS-South

In addition to the HUDF data, we also include the two additional deep parallel fields from the HUDF09 program, as well as all the WFC3/IR data over the GOODS-South field. The latter were taken as part of the ERS program (Windhorst et al. 2011) and the multi-cycle treasury campaign CANDELS (PI: Faber/Ferguson; Grogin et al. 2011; Koekemoer et al. 2011). These data were already used for a $z \sim 10$ search in our previous analysis from Oesch et al. (2012a). We therefore refer the reader to that paper for a more detailed discussion. However, since our previous analysis the acquisition of an additional four epochs of CANDELS DEEP data was completed, resulting in deeper data by about 0.2 mag. These are included now in this paper, which will allow us to further tighten our constraints on the $z \sim 10$ LF.

In the optical, we make use of all ACS data taken over the GOODS South field, which includes additional imaging from supernova follow-up programs. These images reach ~ 0.1 – 0.3 mag deeper than the v2.0 reductions of GOODS, in particular in the z_{850} band. We also reduce and include all the I_{814} data, which were taken over this field. By combining all these datasets, we have produced what is the deepest optical image to date over the GOODS-S field. Such deep optical data are very important for excluding lower-redshift interlopers in LBG samples.

For constraints from *Spitzer*/IRAC, we use the public data from the GOODS campaign. These exposures are 23 hr deep and reach to ~ 26 mag (M. Dickinson et al., in preparation). All these fields are also outlined in Figure 1.

3. SAMPLE SELECTION

Source catalogs are obtained with SExtractor (Bertin & Arnouts 1996), which is run in dual image mode with a specific detection image, depending on the galaxy sample we are interested in. For all samples at $z < 10.5$, we use a χ^2 detection image (Szalay et al. 1999) based on the JH_{140} and H_{160} bands. For $z > 10$ JH_{140} -dropout selections we use the H_{160} band for source detection.

All images are matched to the same point-spread function (PSF) when performing photometry measurements. Colors are based on small Kron apertures (Kron factor 1.2), typically $0''.2$ radius, while magnitudes are derived from large apertures using the standard Kron factor of 2.5, typically $0''.4$ radius. An additional correction to total fluxes is performed based on the encircled flux measurements of stars in the H_{160} band to account for flux loss in the PSF wings. This correction is typically ~ 0.2 mag, but depends on the actual Kron aperture size of individual galaxies.

3.1. Advantages of Lyman Break over Photometric Redshift Selections

In this paper, we adopt an LBG selection to identify galaxies at $z \gtrsim 8.5$. The major advantages of this approach over a photometric redshift selected sample as is used, e.g., in Ellis et al. (2013) are simplicity and robustness. The Lyman break technique provides a straightforward and robust selection, which is easily reproducible by other teams (e.g., Schenker et al. 2013). Furthermore, the simplicity of the Lyman break color-color criteria also allows for a straightforward estimate of the selection volumes based on simulations.

In contrast, the photometric redshift likelihood functions are heavily dependent on the assumed template set and even on the specific photometric redshift code that is used. Additionally,

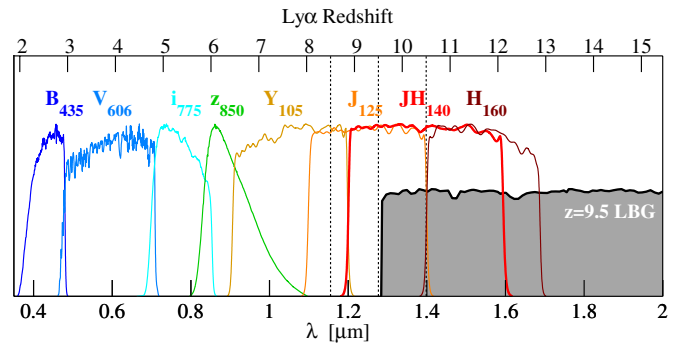


Figure 2. The *HST* filter set over the HUDF12/XDF and the CANDELS fields together with a representative galaxy spectrum at $z = 9.5$. Due to the high neutral fraction in the IGM, essentially all photons shortward of the redshifted Ly α line are absorbed for galaxies at $z > 6$. This effect is used to select such high-redshift sources based on broadband photometry. The redshift of Ly α is indicated on the top axis. The vertical black dotted lines indicate the location of the break at $z = 8.5, 9.5$, and 10.5 .

(A color version of this figure is available in the online journal.)

the photometric redshift likelihood functions depend on largely unknown priors which are needed to account for the number density of intermediate-redshift passive or dusty galaxies. A particular problem is that most high-redshift photometric analyses give equal weight to all templates at all redshift (i.e., they adopt a flat prior). This includes faint galaxies with extreme dust extinction at intermediate redshift or passive sources at $z > 5$, which are unlikely to be very abundant in reality.

A further uncertainty, in particular for high-redshift sources, is how undetected fluxes are treated in the fitting process. This can have significant influence on the lower-redshift likelihood estimates.

Given all these advantages, we will therefore select high-redshift galaxies using the Lyman break technique and we will determine their photometric redshifts a posteriori using standard template fitting on this pre-selected sample of LBGs.

3.2. $z \sim 9$ Lyman Break Selection

The addition of deep F140W imaging data over the HUDF gives us the ability to select new samples of $z \sim 9$ galaxies over that field. As can be seen in Figure 2, the absorption due to the intergalactic neutral hydrogen shifts in between the Y_{105} and J_{125} filters at $z \gtrsim 9$. For a robust Lyman break selection, we thus combine the Y_{105} and J_{125} filter fluxes in which galaxies start to disappear at $z \sim 9$. Our adopted selection criteria are

$$(Y_{105} + J_{125})/2 - JH_{140} > 0.75 \quad (1)$$

$$(Y_{105} + J_{125})/2 - JH_{140} > 0.75 + 1.3 \times (JH_{140} - H_{160})$$

$$S/N(B_{435} \text{ to } z_{850}) < 2 \wedge \chi^2_{\text{opt}} < 2.8.$$

These criteria (shown in Figure 3) are chosen to select sources at $z \sim 8.5$ – 9.5 . We additionally use a $(J_{125} - H_{160}) < 1.2$ criterion to cleanly distinguish our $z \sim 9$ and $z \sim 10$ samples (see next section).

We only include sources which are significantly detected in the H_{160} and JH_{140} images with at least 3σ in each filter and with 3.5σ in at least one of the two. As a cross-check we selected sources based on an inverse-variance weighted combination of the J_{125} , JH_{140} , and H_{160} images at 5σ . Both selections resulted in the same final sample of high-redshift sources, i.e., all selected candidates are $> 5\sigma$ detections.

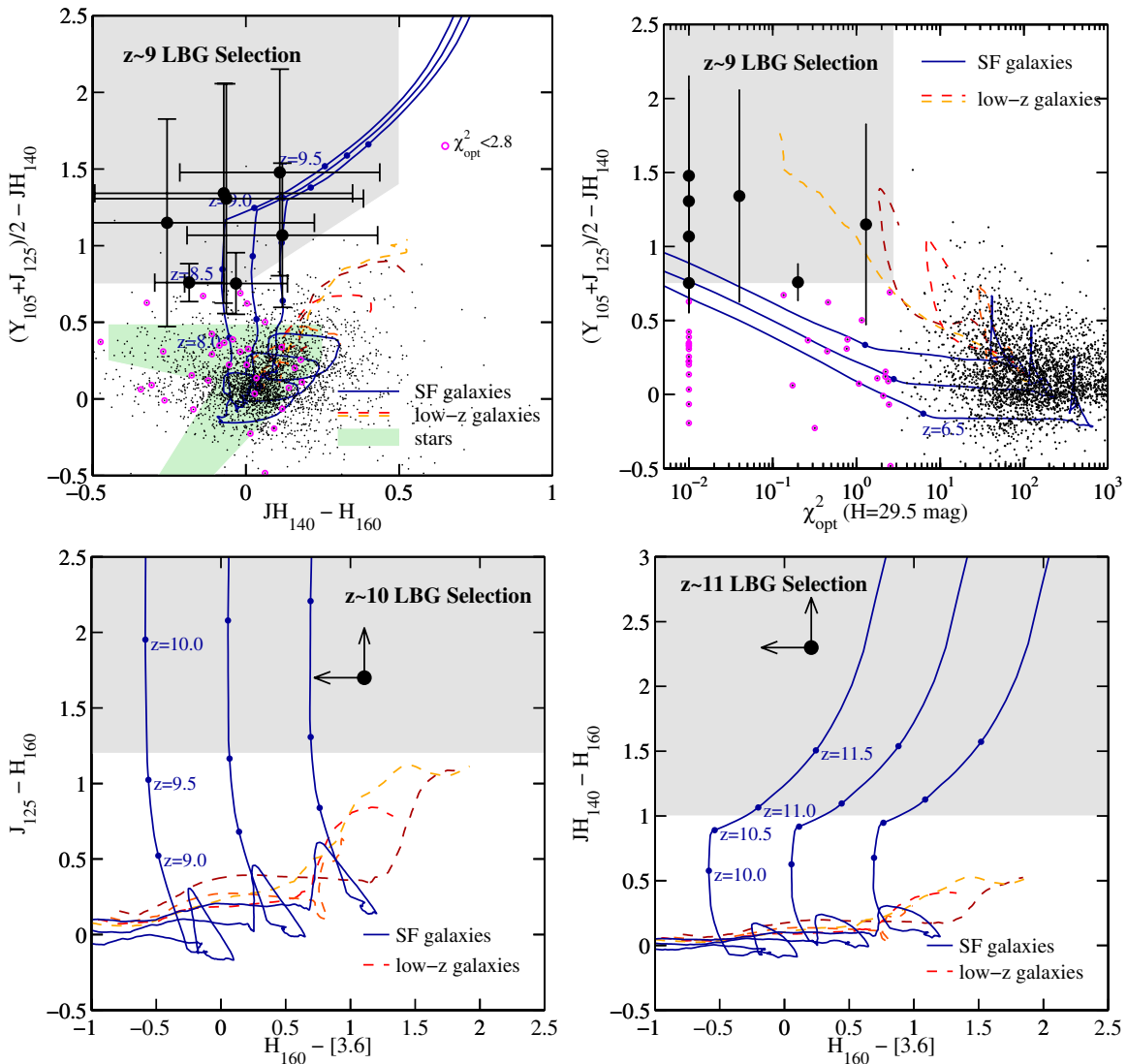


Figure 3. The different color-color selections of our LBG samples. For the $z \sim 9$ sample, we average the Y_{105} and J_{125} flux measurements to provide for a clean dropout selection which separates low-redshift galaxies (dashed yellow to red lines) from star-forming sources at high redshift (blue). The different SF tracks assume a dust extinction of $E(B - V) = 0, 0.15, 0.30$ mag using a Calzetti et al. (2000) reddening. In all panels, the color selections are indicated as light gray regions. The small black dots (in upper panels) show the full galaxy sample, while the large filled black circles represent the high- z candidate sample. Small magenta circles in the upper panels represent galaxies with $\chi^2_{\text{opt}} < 2.8$. As can be seen from their color distribution, the most likely sources to scatter into the $z \sim 9$ selection are blue sources at just somewhat lower redshift ($z \sim 7-8$) rather than intermediate-redshift passive galaxies (yellow line at $JH_{140} - H_{160} > 0.2$). The upper right panel illustrates the χ^2_{opt} criterion for the $z \sim 9$ selection, which guards our sample against $z < 7$ sources. Sources with $\chi^2_{\text{opt}} < 0.01$ are limited at that value. As can be seen, the $z \sim 9$ candidates lie in a quite unique region in the color- χ^2_{opt} plot, with only a few sources just outside our selection window. For the higher-redshift samples (lower left and right panel), the primary selection criterion is the red color in the WFC3/IR filters. However, we additionally check for strong detections in both IRAC bands ([3.6] and [4.5]). The limits on colors are 1σ .

(A color version of this figure is available in the online journal.)

In addition to the color selections, we require sources to be undetected at shorter wavelengths. In particular, we use 2σ non-detection criteria in all optical bands individually. Furthermore, we adopt an optical pseudo- χ^2 constraint. This is defined as $\chi^2_{\text{opt}} = \sum_i \text{SGN}(f_i)(f_i/\sigma_i)^2$. The summation runs over all the optical filter bands B_{435} , V_{606} , i_{775} , I_{814} , and z_{850} , and SGN is the sign function, i.e., $\text{SGN}(x) = -1$ if $x < 0$ and $\text{SGN}(x) = 1$ if $x > 0$. This measure allows us to make full use of all information in the optical data. We only consider galaxies with $\chi^2_{\text{opt}} < 2.8$. This cut reduces the contamination rate by a factor $\sim 3\times$, while it only reduces the selection volume of real sources by 20% (see also Oesch et al. 2012b). This is a powerful tool for providing source lists with low contamination rates (see also Section 3.5.2).

These selection criteria result in seven $z \sim 9$ galaxy candidates in the HUDF12/XDF dataset. These sources are listed in Table 2 and their images are shown in Figure 4. In Figure 5, we additionally show the spectral energy distribution (SED) fits and redshift likelihood functions for these sources. For comparison, these are derived from two photometric redshift codes, ZEBRA (Feldmann et al. 2006; Oesch et al. 2010b) as well as EAZY (Brammer et al. 2008). As is evident, the vast majority of sources do show a prominent peak at $z \sim 8-9$ together with a secondary, lower likelihood peak at $z \sim 2$. The best-fit photometric redshifts of these candidates range between $z = 8.1$ and 9.0 , with the exception of one source (XDFyj-39446317), which has a ZEBRA photometric redshift of only $z_{\text{phot}} = 2.2$. However, using the EAZY code and template set, the best-fit redshift is

Table 2
Photometry of $z > 8$ LBG Candidates in the HUDF12/XDF Data

ID	R.A. z_{EBRA} z_{phot}	Decl. z_{EAZY} z_{phot}	H_{160}	$(YJ) - JH_{140}$	$J_{125} - H_{160}$	$JH_{140} - H_{160}$ Comments	$S/N_{H_{160}}$	$S/N_{JH_{140}}$	$S/N_{J_{125}}$	χ^2_{opt}
$z \sim 9$ YJ -dropouts										
XDFyj-38135540	03:32:38.13 8.4 $^{+0.1}_{-0.1}$	-27:45:54.0 8.4 $^{+0.1}_{-0.2}$	27.95 \pm 0.10	0.8 \pm 0.1	0.0 \pm 0.1	-0.2 \pm 0.1	13.1	16.0	9.8	0.2
Bouwens UDFy-38125539; McLure HUDF12-3813-5540 ($z = 8.3$); and in other Y -dropout samples.										
XDFyj-39478076	03:32:39.47 8.1 $^{+0.3}_{-0.6}$	-27:48:07.6 8.3 $^{+0.2}_{-0.5}$	28.53 \pm 0.14	0.8 \pm 0.2	0.4 \pm 0.2	-0.0 \pm 0.2	8.7	9.7	5.0	-0.6
Bouwens UDFy-39468075; Ellis HUDF12-3947-8076 ($z = 8.6$)										
XDFyj-39216322	03:32:39.21 8.8 $^{+0.5}_{-0.5}$	-27:46:32.2 8.9 $^{+0.5}_{-0.4}$	29.49 \pm 0.25	1.1 \pm 0.5	0.3 \pm 0.4	0.1 \pm 0.3	5.1	4.9	3.2	-1.4
Ellis HUDF12-3921-6322 ($z = 8.8$)										
XDFyj-42647049	03:32:42.64 9.0 $^{+0.5}_{-0.5}$	-27:47:04.9 9.2 $^{+0.5}_{-0.6}$	29.15 \pm 0.21	1.5 \pm 0.7	0.8 \pm 0.6	0.1 \pm 0.3	4.4	4.9	2.1	-0.5
Ellis HUDF12-4265-7049 ($z = 9.5$)										
XDFyj-40248004	03:32:40.24 8.8 $^{+0.5}_{-0.5}$	-27:48:00.4 8.9 $^{+0.6}_{-0.3}$	29.87 \pm 0.30	1.3 \pm 0.7	0.3 \pm 0.6	-0.1 \pm 0.4	3.5	3.3	2.2	0.0
Faint source. Not in Ellis et al. (2013) sample.										
XDFyj-43456547	03:32:43.45 8.7 $^{+0.6}_{-0.5}$	-27:46:54.7 8.9 $^{+0.7}_{-0.8}$	29.69 \pm 0.42	1.3 \pm 0.7	0.5 \pm 0.7	-0.1 \pm 0.4	3.1	3.5	1.8	-3.8
Ellis HUDF12-4344-6547 ($z = 8.8$)										
XDFyj-39446317 ^a	03:32:39.44 2.2 $^{+0.8}_{-0.7}$	-27:46:31.7 8.6 $^{+1.0}_{-1.5}$	29.77 \pm 0.27	1.1 \pm 0.7	>1.0	-0.3 \pm 0.5	3.8	3.7	1.3	1.3
Faint source. Very wide $p(z)$, with low best-fit redshift. Not in Ellis et al. (2013) sample.										
$z \sim 10$ J -dropouts										
XDFj-38126243	03:32:38.12 9.8 $^{+0.6}_{-0.6}$	-27:46:24.3 9.9 $^{+0.7}_{-0.6}$	29.87 \pm 0.40	>1.9	1.4 \pm 0.9	0.3 \pm 0.4	5.8	3.4	1.2	-0.6
This source was selected as a $z \sim 10$ candidate in the HUDF09 year 1 data, but did not appear in final Bouwens et al. (2011a) sample due to low S/N in second year data (see Figure 6).										
$z \sim 10.7$ JH -dropouts										
XDFjh-39546284	03:32:39.54 11.8 $^{+0.2}_{-0.4}$	-27:46:28.4 11.9 $^{+0.2}_{-0.5}$	28.55 \pm 0.14	...	>2.3	>2.3	7.3	0.2	-1.6	0.8
UDFj-39546284 of Bouwens et al. (2011a), Oesch et al. (2012a); Ellis HUDF12-3954-6284 ($z = 11.9$)										

Notes. S/N are measured in circular apertures of fixed 0".35 diameter.

^a Due to the low photometric redshift estimate, we do not include the source XDFyj-39446317 in our analysis of the UV LF at $z \sim 9$. One contaminating lower-redshift source is expected in our sample due to photometric scatter (see Section 3.5.2).

found at $z = 8.6$. The photometric redshift likelihood function for this source is very wide using both codes.

From photometric scatter simulations (see Section 3.5.2), we expect to find 0.9–1.1 low-redshift contaminants in our $z \sim 9$ sample due to photometric uncertainties. Therefore, finding an LBG candidate with such a low redshift is not necessarily unexpected. We will thus list it as a possible candidate in Table 2. However, we will exclude XDFyj-39446317 from our determination of the UV LF at $z \sim 9$.

Note that Ellis et al. (2013) and McLure et al. (2013) performed a photometric redshift selection of $z \gtrsim 8.5$ sources over the same field, which we discuss in detail in Section 3.7.3.

3.3. The $z \sim 10$ Lyman Break Selection

Galaxies at redshifts approaching $z \sim 10$ start to disappear in the J_{125} filter. Following Bouwens et al. (2011a) and Oesch et al. (2012a), we select $z \sim 10$ galaxies based on very red $J_{125} - H_{160}$ colors and we use *Spitzer*/IRAC photometry to guard this selection against intermediate-redshift extremely dusty and evolved galaxies in a second step. This selection process also used JH_{140} data when available (i.e., over the HUDF12/XDF field), and was used for all the datasets shown in Figure 1.

The *HST* selection criteria are

$$(J_{125} - H_{160}) > 1.2 \wedge (JH_{140} - H_{160}) < 1.0 \quad (2)$$

$$S/N(B_{435} \text{ to } Y_{105}) < 2 \wedge \chi^2_{\text{opt}} < 2.8$$

in addition to at least 3σ detections in both H_{160} and JH_{140} and $>3.5\sigma$ in one of these. All sources in our final list also satisfy a $>5\sigma$ detection criterion in the combined $J_{125} + JH_{140} + H_{160}$ image.

The $JH_{140} - H_{160}$ color criterion was introduced to distinguish $z \sim 10$ from $z \sim 11$ galaxies over the HUDF12/XDF field. The other fields, which do not have deep JH_{140} imaging, do not include this criterion. We account for this difference in our analysis of the selection functions (Section 3.6).

When applying these selection criteria to the WFC3/IR+ACS data over GOODS-S, we previously identified 16 galaxies which satisfied these criteria. However, these are all extremely bright in the *Spitzer*/IRAC bands and are even detectable in the shallow [5.8] and [8.0] channel data over GOODS-S (having $H_{160} - [5.8] = 2.4\text{--}4.0$ mag). These sources were therefore excluded from our $z \sim 10$ analysis, as their H_{160} to IRAC colors were too red for a genuine $z \sim 10$ galaxy. These are most likely $z \sim 2\text{--}3$ galaxies with significant extinction and possibly evolved stellar populations (see Oesch et al. 2012a).

Even taking advantage of the deeper WFC3/IR data that became available over the CANDELS-South field subsequent to the Oesch et al. (2012a) analysis, no new credible $z \sim 10$ source could be found. However, our selection revealed three potential sources in the HUDF12/XDF data. Unfortunately, two of these are very close to a bright, clumpy foreground galaxy. Their photometry is therefore very uncertain, and it is unlikely that they are real high-redshift sources. We nevertheless

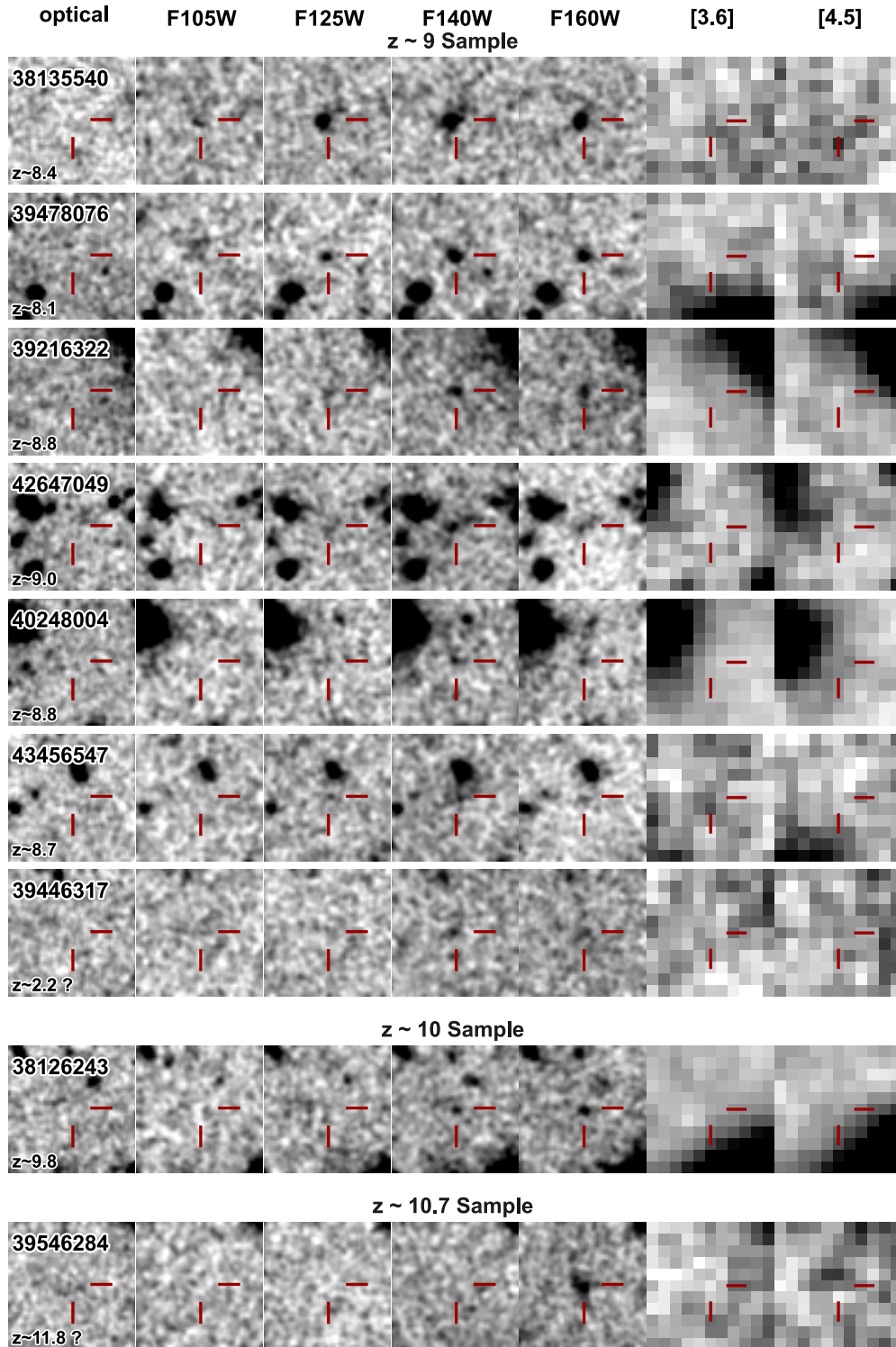


Figure 4. $3'' \times 3''$ images of the $z > 8$ galaxy candidates. From left to right, the images show a stack of all optical bands, Y_{105} , JH_{140} , J_{125} , H_{160} , IRAC [3.6], and [4.5]. The stamps are sorted by dropout sample. The approximate photometric redshift of each source is shown in the lower left corner of the optical stacked stamp (see also Table 2).

(A color version of this figure is available in the online journal.)

list these as potential sources in Table 6. However, we will not use them in the subsequent analysis.

This leaves us with only one likely $z \sim 10$ galaxy candidate in all the fields we have analyzed here. This is XDFj-38126243, which we had previously identified in the first-epoch data of the HUDF09 as a potential $z \sim 10$ candidate (Bouwens et al. 2011a). However, it was not detected at a significant enough

level in the subsequent second epoch H_{160} data to indicate at high confidence that it was real. As a result it was not included in our final sample of $z \sim 10$ sources from the HUDF09 data.

The source XDFj-38126243 is now clearly detected both in the new H_{160} and in the JH_{140} data from the HUDF12 survey, which clearly confirms its reality. This is demonstrated in Figure 6. As can also be seen from that figure, the source

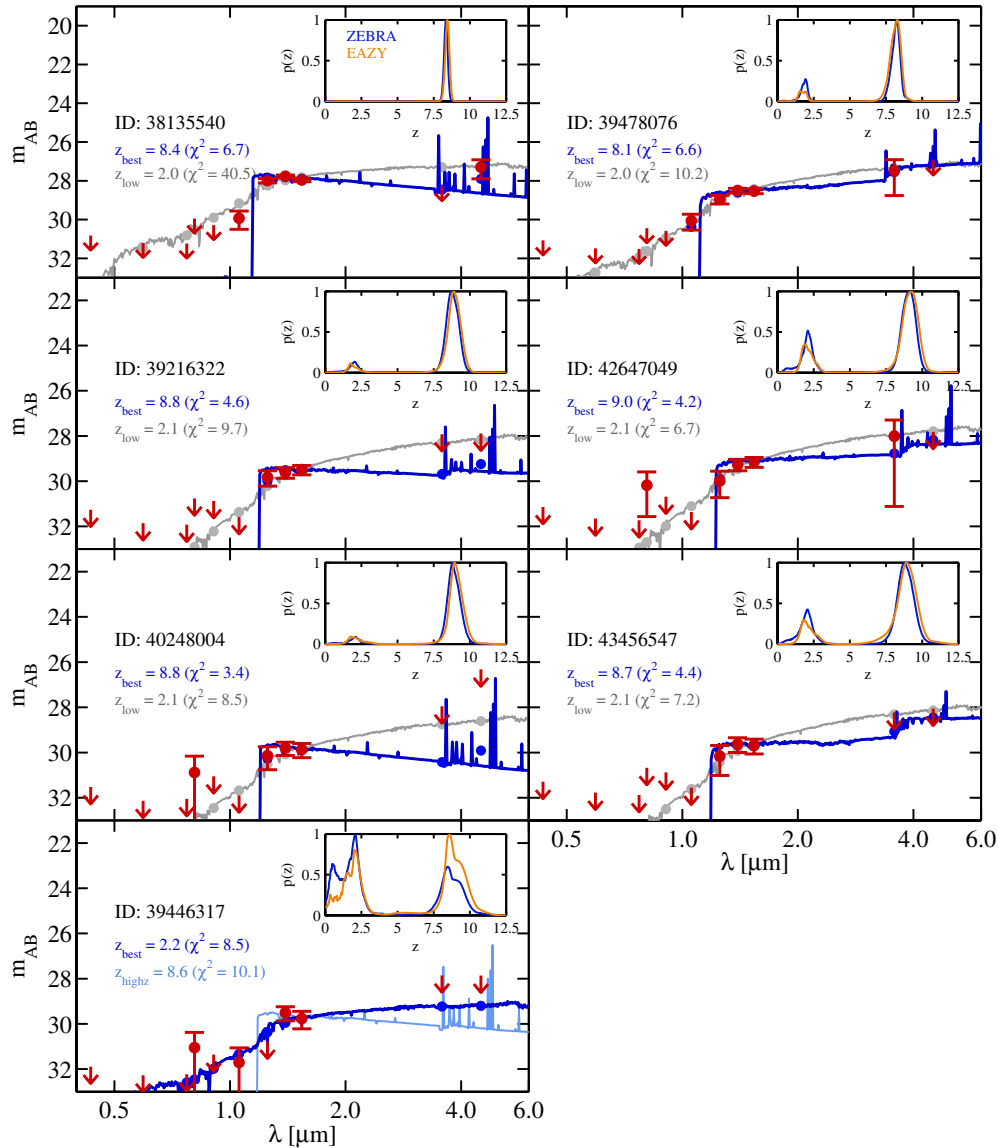


Figure 5. Spectral energy distribution fits to the fluxes of the $z \sim 9$ YJ-dropout candidate galaxies in our sample. The magnitude measurements and upper limits (1σ) are shown in red. These also include self-consistent flux measurements in IRAC [3.6] and [4.5]. The uncertainties we derive for the IRAC fluxes account for the uncertainties involved in removing contamination from neighboring sources, resulting in some variation in the effective depth of the IRAC data. The best-fit SEDs (blue) as well as the best low-redshift solution (gray) are shown as solid lines. The SED magnitudes are indicated as filled circles. With the exception of source XDFj-39446317 all sources have best-fit redshifts at $z \simeq 8\text{--}9.5$. The low-redshift solutions are evolved galaxies at $z \sim 2$, for which the Lyman break is confused with the Balmer/4000 Å break. As is evident, almost all other sources show a non-negligible secondary peak in their redshift likelihood distribution around $z \sim 2$. Due to the best-fitting low-redshift solution of XDFj-39446317, we do not include this source in our analysis of the UV LF and SFRD. One such source of contamination is completely consistent with our expectation from photometric scatter simulations (see Section 3.5.2).

(A color version of this figure is available in the online journal.)

is extremely compact, consistent with being a point source. We can therefore not exclude that this source is powered by an active galactic nucleus (AGN), which could also explain the possible variability over a timescale of 1 yr (see lower panel of Figure 6). However, the low flux measurement in the second-year HUDF09 data is still consistent with expectations from Gaussian noise. Taken together, the flux measurements of all three epochs are consistent with the source showing no time variability ($\chi^2 = 2.6$).

The source is not detected in our ultra-deep IRAC data, and its colors place it at a photometric redshift of $9.8^{+0.6}_{-0.6}$ (see also Table 2 and Figure 7).

For completeness, we also list three additional potential candidates in the Appendix (see Table 6). These sources lie very close to bright foreground galaxies. Formally, they show colors

consistent with being at very high redshift. However, they are significantly blended with their neighbors, such that the fluxes of these sources cannot be accurately measured with SExtractor, without a more sophisticated neighbor subtraction technique. Additionally, the close proximity to very bright foreground sources casts significant doubt on the reality of these sources, and we therefore do not include these in our analysis.

3.4. $z \sim 10.7$ Lyman Break Selection

The addition of JH_{140} imaging from the HUDF12 data also allows for the selection of $z \gtrsim 10.5$ galaxies based on a red $JH_{140} - H_{160}$ color, as the intergalactic medium (IGM) absorption shifts through the center of the JH_{140} filter (see Figure 3). We therefore search for galaxies in the HUDF12/

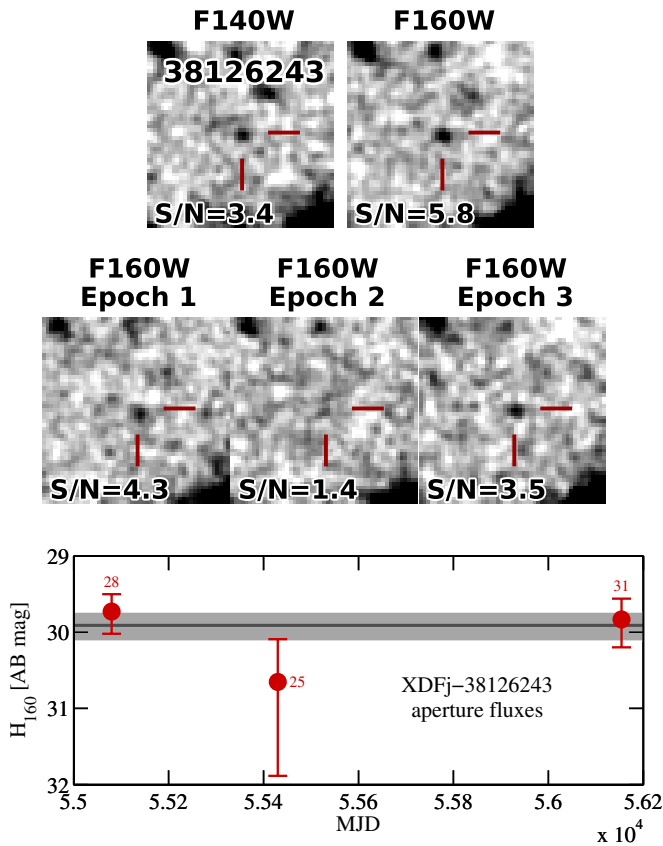


Figure 6. Top: stamps ($3''$ by $3''$) of the $z \sim 10$ candidate XDFj-38126243—which is likely the highest-redshift source over the HUDF12/XDF. The top two stamps are the JH_{140} and H_{160} observations. The H_{160} stack is also split in observations at three different epochs, shown in the bottom three stamps. “Epoch 1” corresponds to the HUDF09 year 1 data (28 orbits), “Epoch 2” are the HUDF09 year 2 data (25 orbits), and “Epoch 3” are the remaining 31 orbits from the HUDF12 and CANDELS observations. The S/N in each band is listed in the lower left. This source was initially selected as a high-redshift candidate after the first year HUDF09 data (Bouwens et al. 2011a). However, as can be seen, the galaxy was only very weakly detected (1.4σ) in the HUDF09 year 2 data. Nevertheless, the source is clearly visible at $\gtrsim 3.5\sigma$ in all other epochs, as well as in the JH_{140} data (only taken from the HUDF12 program). The source is therefore clearly real. The lower signal detection in the “Epoch 2” data is still consistent with the expectation from a Gaussian noise distribution. Bottom: the H_{160} magnitude measurement for the three different epochs. The number of orbits going into each image is indicated close to each datapoint. The fluxes are measured in a circular aperture of $0''.35$ diameter. The magnitude from the total 84-orbit H_{160} image is indicated by the gray line, with errorbars represented by the filled gray area. The flux measurements are consistent with no variability in this source ($\chi^2 = 2.6$). However, an AGN contribution to its UV flux cannot be excluded.

(A color version of this figure is available in the online journal.)

XDF data satisfying the following:

$$(JH_{140} - H_{160}) > 1.0 \quad (3)$$

$$S/N(B_{435} \text{ to } J_{125}) < 2 \wedge \chi_{\text{opt}}^2 < 2.8.$$

In order to ensure the reality of sources in this single-band detection sample, we require $>5\sigma$ detections in H_{160} .

Only one source satisfies these criteria: XDFjh-39546284. This is our previous highest-redshift candidate from the HUDF09 data (UDFj-39546284; see Bouwens et al. 2011a). Surprisingly, with $JH_{140} - H_{160} > 2.3$ it has an extremely red color in these largely overlapping filters. It is by far the reddest

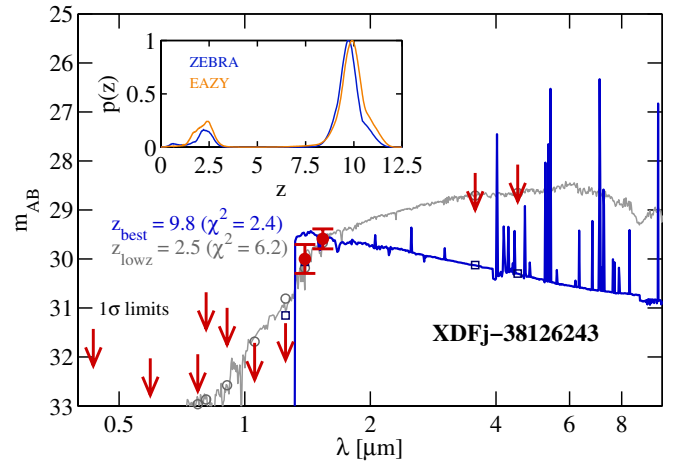


Figure 7. Spectral energy distribution (SED) fit to the fluxes of the galaxy XDFj-38126243. The best-fit redshift is found at $z = 9.8$, which is represented by the blue line. The gray SED corresponds to the best low-redshift solution at $z = 2.5$. Open blue squares and gray circles show the expected magnitudes of these SEDs. 1σ upper limits to undetected fluxes are shown as red arrows. The inset shows the redshift likelihood function as estimated with ZEBRA (blue) and EAZY (orange). Both photometric redshift codes consistently find a prominent peak at $z = 9.8$ and a lower-significance peak at $z = 2.5$.

(A color version of this figure is available in the online journal.)

source in the HUDF12/XDF data, and its rather dramatic color raises some questions.

At face value, the extreme color, together with the non-detection in the optical data and in our deep IRAC imaging, results in a best-fit redshift of $z = 11.8 \pm 0.3$ for this source. However, such a high redshift would imply that the source is $\sim 20\times$ brighter than expected for $z \sim 12$ sources at the same number density (see Bouwens et al. 2012d). While a strong $\text{Ly}\alpha$ emission line could reduce the remarkably high continuum brightness, the lack of $\text{Ly}\alpha$ seen in galaxies within the reionization epoch at $z \gtrsim 6$ indicates that the high fraction of neutral hydrogen in the universe at early times absorbs the majority of $\text{Ly}\alpha$ photons of these galaxies (e.g., Schenker et al. 2012; Pentericci et al. 2011; Caruana et al. 2012; Bunker et al. 2013). Seeing strong $\text{Ly}\alpha$ emission from a source at $z \sim 12$ during the early phase of reionization is particularly unexpected (although perhaps not impossible).

Alternatively, the source could be a $z \sim 2$ extreme line emitter. An emission line at $\sim 1.6\mu\text{m}$ would have to produce the majority of its H_{160} flux, which would require extreme equivalent widths. A possible example of such a source is presented in Brammer et al. (2013). For more extensive discussions of these alternative options for this source see Brammer et al. (2013) and Bouwens et al. (2012d).

Given the uncertain nature of this source, we will treat its detection as an upper limit of ≤ 1 source in the following analysis, and we will only derive upper limits on the luminosity and SFRDs at $z \sim 10.7$ from this single-source sample.

3.5. Sources of Sample Contamination

In the following sections we discuss possible contamination of our $z > 8$ LBG samples.

3.5.1. Dusty and Evolved Galaxies

As already pointed out in Oesch et al. (2012a), galaxies with strong Balmer breaks, or with high dust obscuration, are a potential source of contamination for $z > 9$ galaxy searches.

In particular, in fields with limited depth in the WFC3/IR and optical data, such extremely red sources can remain undetected shortward of H_{160} and can thus satisfy the *HST* selection criteria. Fortunately, with the availability of *Spitzer*/IRAC over all the search fields in this study, such sources can readily be excluded from the samples based on an $H_{160} - [3.6] < 2$ color criterion.

As shown in Oesch et al. (2012a), the CANDELS data contain 16 intermediate brightness sources which satisfy our $z \sim 10$ J_{125} -dropout selections. However, these could all be excluded based on the IRAC constraints. They are all found at $H_{160} \sim 24$ – 26 mag, which suggests that such red, lower-redshift galaxies show a peaked LF. Therefore, it is expected that they would be much less of a problem as contaminants in our fainter samples.

Given this expectation, it is particularly interesting that we actually did not find the lower-luminosity counterparts of such sources in any of the three deep fields, even though our IRAC data are sensitive enough thanks to the IUDF program. Although the survey volume of our deep data is limited, this further suggests that such red galaxies are indeed very rare at lower luminosities. It remains an open and interesting question as to the nature and redshift of these red $H_{160} \sim 24$ – 26 mag galaxies (the redshift is expected to be low, i.e., $z \sim 1$ – 3 , but exactly over what redshift range they are seen is still quite uncertain).

3.5.2. Photometric Scatter of Low- z Sources

After excluding contamination from intermediate-redshift, red galaxies, the next most important source of contamination is photometric scatter. Photometric scatter can cause faint, low-redshift sources to have colors and magnitudes such that they would be selected in our sample. We estimate the magnitude of this effect with simulations using real galaxies based on our photometric catalogs.

In particular, we select all sources with H_{160} magnitudes in the range 24–25 and we rescale their fluxes and apply the appropriate amount of photometric scatter as observed for real sources at fainter luminosities. We then apply our selection criteria to these simulated catalogs in order to estimate the contamination fraction. This is repeated 5000 times, which results in reliably measured contamination fractions.

As expected, contamination due to photometric scatter is most significant at the faint end of our sample. The above simulations show that we do not expect to see any contaminant at >1 mag from the detection limit. In the HUDF12/XDF $z \sim 9$ galaxy sample, we find that 0.9 contaminants are expected per simulation. Given that we find seven sources, this signifies a $\sim 12\%$ contamination fraction. Note that this would have been a factor $3\times$ higher (2.6 contaminants expected) had we not included our optical χ^2 measurement. Again this shows clearly the power of having deep shorter-wavelength data, and the effectiveness with which data over a range of wavelengths can be used.

For the higher-redshift samples, we estimate 0.2 and <0.1 contaminants in the HUDF12/XDF LBG selection at $z \sim 10$ and $z \sim 10.7$, respectively, from analogous simulations. Overall, our extensive simulations show that the contamination due to photometric scatter is thus expected to be $\lesssim 20\%$ for all these samples.

As an additional test of the contamination rate in our samples, we can use the best-fitting low-redshift SEDs for our $z \sim 9$ candidates in order to estimate with what probability such types of galaxies would be selected as LBGs. In particular, we use the expected magnitudes of the $z \sim 2$ SED fits shown in Figure 5,

perturb these with the appropriate photometric scatter, and apply our $z \sim 9$ LBG selection. We repeat this simulation 10^6 times for each of our $z \sim 9$ galaxy candidates, which allows us to estimate the probability for our $z \sim 9$ sample to contain a certain number of contaminants. We find that at 65% confidence, our sample contains zero or one contaminant, while ≤ 2 contaminants are found in 90% of the realizations. Finally, the chance that the majority (i.e., >3) of these $z \sim 9$ candidates lie at $z \sim 2$ is estimated to be $<1.5\%$.

Note that the average number of contaminants per realization is found to be 1.1, i.e., very similar to our previous estimate of 0.9 contaminants based on using the real, bright galaxy population. It should be noted that the SED-based test makes no assumptions about the relative abundance of faint, star-forming $z > 8$ galaxies and the possible intermediate-redshift passive sources at the same observed magnitude (~ 29 mag AB). Both observationally and theoretically, the number density of low-mass, passive galaxies at $z \gtrsim 2$ is still very poorly understood, making it very difficult to gauge the contamination rates for our $z > 8$ samples. In particular, these passive $z \sim 2$ galaxies would need to have only $(1-3) \times 10^8 M_\odot$ and $M_B = -15$ to -16 mag.

Nevertheless, these tests show that while we cannot completely exclude intermediate-redshift contamination in our samples, the majority of our candidates are clearly expected to lie at $z > 8$. As we noted earlier, to account for this contamination we exclude the $z \sim 9$ candidate XDFyj-39446317 from the subsequent analysis, in agreement with its ambiguous photometric redshift at $z = 2.2$ or $z = 8.6$.

3.5.3. Additional Sources of Contamination

Galactic dwarf stars can be a significant concern for $z \sim 7$ – 8 galaxy samples, due to strong absorption features in their atmospheres, which causes their intrinsic colors to overlap with the high-redshift galaxy selection criteria. However, this is not as much of a concern at $z > 9$. Stellar spectra are significantly bluer in our selection colors than high-redshift galaxies. This can be seen in Figure 3, where we plot the location of the stellar sequence including M, L, and T dwarfs. Stars with intrinsically red colors are therefore not expected to be a significant contaminant in our samples. The only possibility for such stars to contaminate our selection is due to photometric scatter, which we implicitly accounted for in our photometric simulations in the previous section.

Additionally, we can exclude contamination by supernovae. We verified that all galaxies in our sample are detected at statistically consistent signal-to-noise (S/N) levels in the images taken over a time baseline of about 3 yr as part of the HUDF09 and HUDF12 campaigns.

For a more extensive review of possible contamination in $z \gtrsim 8$ samples, see also Coe et al. (2013) and Bouwens et al. (2011b).

3.6. Redshift Selection Functions

The expected redshift distributions of our LBG samples are estimated based on extensive simulations of artificial galaxies inserted in the real data, which are then re-selected in the same manner as the original sources (see also Oesch et al. 2007, 2012a). In particular, we estimate the completeness $C(m)$ and selection probabilities $S(z, m)$ as a function of H_{160} magnitude m and redshift z .

Following Bouwens et al. (2003), we use the profiles of $z \sim 4$ LBGs from the HUDF and GOODS observations as templates for these simulations. The images of these sources are scaled

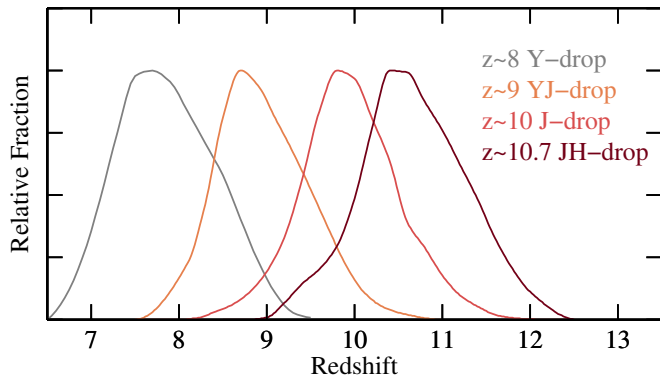


Figure 8. The redshift selection function for different LBG samples. The new selections used in this paper nicely extend the lower-redshift Y -dropout samples. The new YJ -dropout selection has a mean redshift $z = 9.0$, while the J -dropout sample is expected to lie at a mean $z = 10.0$. Although the $JH_{140} - H_{160} > 1$ color is only satisfied for $z > 11$ galaxies, the JH_{140} -dropout sample extends to significantly lower redshift, and peaks only at $z \sim 10.6$. This is mainly due to photometric scatter and due to the relatively slow change in $JH_{140} - H_{160}$ color from $z \sim 10$ –11 (see Figure 3).

(A color version of this figure is available in the online journal.)

to account for the difference in angular diameter distance as well as a size scaling of $(1+z)^{-1}$. The latter is motivated by observational trends of LBG sizes with redshift across $z \sim 3$ –8 (see, e.g., Ferguson et al. 2004; Bouwens et al. 2004; Oesch et al. 2010a; Ono et al. 2012).

The colors of the simulated galaxy population are chosen to follow a distribution of UV continuum slopes with $\beta = -2.4 \pm 0.4$ (see, e.g., Bouwens et al. 2009, 2010; Finkelstein et al. 2010; Stanway et al. 2005), and are modulated by the IGM absorption model of Madau (1995) over a range of redshifts $z = 8$ to $z = 13$. Ten thousand galaxies are simulated for each redshift bin in steps of $dz = 0.2$, which allows for a reliable estimate of the completeness and selection probability taking into account the dispersion between input and output magnitudes.

The result of these simulations enables us to compute the redshift distribution of galaxies after assuming an LF $\phi(M)$

$$p(z) = dN/dz = \int dm \frac{dV}{dz} S(m, z) C(m) \phi(M[m, z]). \quad (4)$$

We assume a baseline UV LF evolution with $\alpha = -1.73$ and $M_*(z) = -20.29 + 0.33 \times (z - 6)$, consistent with the trends found across $z \sim 4$ to $z \sim 8$ (Bouwens et al. 2011b). The normalization is not relevant for the relative distributions. For the K -correction in the conversion from absolute to observed magnitude, we use a 100 Myr old, star-forming template of Bruzual & Charlot (2003).

The results of this calculation are shown in Figure 8. It is clear that the redshift selection functions are significantly wider than the target redshift range based on the simple LBG color tracks shown in Figure 3. The reason for this is simply photometric scatter. The mean redshift (and the width) of our samples are $9.0 (\pm 0.5)$, $10.0 (\pm 0.5)$, and $10.7 (\pm 0.6)$ for the YJ -, J - and JH -dropout samples, respectively.

3.7. Comparison to Previous $z > 8$ Samples

In the following sections, we compare our LBG samples with previous selections over these fields in the literature.

3.7.1. Bouwens et al. (2011a) $z \gtrsim 8.5$ Y -dropouts

In Bouwens et al. (2011a), we already identified three possible sources at $8.5 \lesssim z \lesssim 10$. These sources were identified based on their red $Y_{105} - J_{125}$ colors. With the advent of the HUDF12 data, all these sources are confirmed as valid high-redshift candidates. However, they are all weakly detected in the Y_{105} filter, which results in a somewhat lower estimate on their redshift. Nevertheless, one of these sources (UDFy-38135540) is included in our present $z \sim 9$ sample. The other two (UDFy-37796000 and UDFy-33436598) do have YJ – JH colors of ~ 0.4 , which are too blue to be included in our sample. Their photometric redshifts are 7.8 and 7.7, respectively. The photometries of both these sources are also listed in the Appendix (see Table 6).

As deeper data become available it is not unusual to find that the photometric redshifts undergo small shifts to lower values, also due to the larger number of sources at lower redshifts (Muñoz & Loeb 2008). The original bias to higher redshifts results from the larger photometric scatter in shallower data, resulting in an overestimate of the Lyman break amplitude. Similar biases also affect the photometric redshift samples, e.g., compare the redshift estimates of McLure et al. (2010) with McLure et al. (2013). This is a well-known and well-understood effect and should be expected to affect all redshift estimates derived from photometric data, regardless of the procedures used. This effect explains the question raised by Ellis et al. (2013) regarding the slightly lower redshift for these sources.

3.7.2. Bouwens et al. (2011a) $z \sim 10$ Candidates

In our previous analysis of the full HUDF09 data over the HUDF, we already identified the source XDFjh-39546284 as a probable high-redshift source. Based on those data and on a plausible evolution of the UV LF to higher redshift, we expected this source to lie at $z \sim 10.4$. Surprisingly however, XDFjh-39546284 was not detected in the new JH_{140} data and so its redshift cannot be $z \sim 10.4$ (see also Ellis et al. 2013). Its nature is now unclear. The best-fit $z = 11.8$ solution is quite unlikely, given what we now know about the evolution of the LF at redshifts $z \sim 4$ –9. XDFjh-39546284 is $\sim 20\times$ brighter than expected for a $z \sim 12$ galaxy at its number density (see Figure 4 of Bouwens et al. 2012d). Dramatic changes to higher LDs at $z > 11$ are unlikely, and so this object presents us with an interesting conundrum. This is discussed in detail in Bouwens et al. (2012d) and Brammer et al. (2013).

After the first half of the HUDF09 data were taken over the HUDF in the first year of observations, we had identified three potential $z \sim 10$ sources (see the Supplementary Information/Appendix A of Bouwens et al. 2011a). These sources were selected as J_{125} -dropouts, very similar to the candidates selected in the present analysis. However, the three candidates were not detected at sufficient significance in the second year WFC3/IR H_{160} data, which raised the possibility that they were spurious detections.

With the advent of additional H_{160} data from the HUDF12 survey, we can now confirm that all three sources are in fact real. They are all significantly detected in the full H_{160} and JH_{140} data. However, only one of these sources is now in our $z > 8$ galaxy sample. Two sources show photometric redshifts of $z \sim 8$, given their very faint detections in the Y_{105} data of 0.5σ and 2.3σ , respectively. However, we remark that one of these two sources may still be at $z > 8.5$ given the tentative nature of its Y_{105} -band detection (i.e., 0.5σ). The last source (XDFj-38126243)

remains in our new $z \sim 10$ J_{125} -dropout sample. For this source, we find a photometric redshift of $z = 9.8^{+0.6}_{-0.6}$. With the possible exception of the enigmatic $z \sim 11.8$ redshift candidate (XDFj-39546284), this is therefore the highest-redshift galaxy candidate in the HUDF12/XDF field.

In Figure 6, we show the JH_{140} and H_{160} stamps of the source XDFj-38126243, including splits of the data by epoch. It is clear that the source is real, as it is now detected at 5.8σ in H_{160} and at 3.4σ in JH_{140} . As can be seen, the second year HUDF09 data (Epoch 2) only contain a weak, though statistically consistent, signal of this source. Given that there were just two epochs available at that time and the overall S/N of the source was below our threshold, we did not include this source in the Bouwens et al. (2011a) and Oesch et al. (2012a) analyses.

Also shown in Figure 6 is the best-fit template and photometric redshift distribution for this source. With both photometric redshift codes ZEBRA (Feldmann et al. 2006; Oesch et al. 2010b) and EAZY (Brammer et al. 2008), we find a consistent best-fit photometric redshift at $z = 9.8\text{--}9.9$ with uncertainties of $\Delta z \sim 0.6$ (see Table 2). As expected for such a faint source, the redshift likelihood function shows a lower-redshift peak around $z \sim 2.5$ (gray SED). The integrated low-redshift ($z < 5$) likelihood is 18%. This is consistent with our estimate of lower-redshift contamination due to photometric scatter in our J_{125} -dropout sample. Taken together the data are consistent with this being a viable and likely $z \sim 10$ candidate.

Note that Ellis et al. (2013) do not include this source in their analysis, but they specifically discuss it. They state the source is not significantly detected ($<5\sigma$) in their summed $J_{125} + JH_{140} + H_{160}$ image, for which we see two main reasons. (1) With a photometric redshift of $z \sim 10$, this galaxy is largely redshifted out of the J_{125} band, greatly reducing (by $\sim 30\%$) its detection significance in a $J_{125} + JH_{140} + H_{160}$ stack. Use of a $JH_{140} + H_{160}$ stack is better for such cases and is what we do here. (2) The source is very compact, and therefore it is detected at higher significance in the small apertures we use here for S/N measurements ($0''.35$ diameter) compared to the Ellis et al. (2013) analysis ($0''.47\text{--}0''.50$ diameter). Moreover, we stress that this source is significantly detected in several independent subsets of the data, and is therefore certainly real (see Figure 6).

3.7.3. Ellis et al. (2013) and HUDF12 Team Papers

The HUDF12 team has recently published a sample of seven $z \gtrsim 8.5$ galaxy candidates identified in the HUDF12 data in Ellis et al. (2013). These sources were based on a photometric redshift selection technique (see also McLure et al. 2013), with a $>5\sigma$ detection in $\sim 0''.5$ diameter apertures. Here, we use smaller apertures of $0''.35$ diameter for S/N measurements, which in most cases are more optimal for the very small $z \sim 9\text{--}10$ sources, and result in a small additional gain of $\sim 20\%$ in S/N. This is why we could expect to find additional sources in our sample compared to Ellis et al. (2013).

In general, our sample is in very good agreement with the selection of Ellis et al. (2013). With the exception of two, we include all their sources in our $z > 8$ samples. The discrepant ones are UDF12-3895-7114 and UDF12-4106-7304, which we discuss below. Their photometry is additionally listed in the Appendix (see Table 6).

UDF12-3895-7114. This source certainly shows colors very similar to a $z > 8$ candidate. However, we measure $(YJ) - JH_{140} = 0.5 \pm 0.5$, which is bluer than our selection color for the $z \sim 9$ sample. Hence, it is not included in our $z \sim 9$ sample. While Ellis et al. (2013) find a best-fit photometric

redshift of 8.6 ± 0.7 , the source is not present in the “robust” sample of McLure et al. (2013), and we find a photometric redshift distribution function which is very broad, with a best fit at $z \sim 0.5$ (using both ZEBRA or EAZY). This different result compared to the Ellis et al. (2013) redshift estimate may be caused by small uncertainties in the photometry measurements (given that we also use different apertures). Additionally, we perform IRAC flux measurements on a source-by-source basis. These include an additional uncertainty due to the subtraction of neighboring sources (see, e.g., Labbé et al. 2010, 2012). This is not the case in the Ellis et al. (2013) analysis, who note that they use constant upper limits on the IRAC fluxes.

As we have discussed, photometric redshifts are very uncertain for sources this faint and so there is a chance that this source is still at $z > 8$. Nevertheless, our analysis raises significant doubt about its high-redshift nature.

UDF12-4106-7304. The WFC3/IR PSF shows significant diffraction spikes, which are caused by the mount of the secondary mirror. While typically only seen around bright stars, these diffraction spikes are so strong that they can also emanate from compact foreground galaxies, particularly in the redder WFC3/IR filters. The source UDF12-4106-7304 of Ellis et al. (2013) is located at the edge of such a diffraction spike for both the H_{160} and the JH_{140} filters (the only filters wherein UDF12-4106-7304 is significantly detected). This is shown in Figure 9. The photometry of this source is clearly significantly enhanced by the diffraction spike. The detection significance of UDF12-4106-7304 is critically reduced once the diffraction spike signal is removed. The profile of the bright foreground galaxy is non-trivial to model, but fortunately only its core is relevant for causing the diffraction spikes. We therefore use galfit (Peng et al. 2002) to model the center of this source and subtract the diffraction spikes that were scaled to match the core flux. Doing so results in the flux of UDF12-4106-7304 being reduced by a factor $\sim 2\times$, in both JH_{140} and H_{160} , which makes it only a 2.8σ total NIR detection. This is too low to be included in a robust sample.

Additional uncertainty about the reality of this source arises due to its different morphology in the H_{160} and JH_{140} images. The “source” also lies close to another faint foreground galaxy. It is therefore not clear whether the diffraction spike and the neighboring galaxy conspired to lead to the detection of this potential candidate. In any case, for these reasons, and for the low detection flux, the reality of UDF12-4106-7304 remains in question and we do not include this source in our analysis.

4. RESULTS

4.1. The Abundance of $z > 8$ Galaxies

The sample of nine $z > 8$ galaxy candidates we compiled in the previous sections allows us to make some of the first estimates of the $z \sim 9\text{--}11$ UV LFs. Although limited in area, the HUDF12/XDF data alone provide very useful constraints already at $z \sim 9$ and limits at $z \sim 11$. Additionally, due to the deeper data over the HUDF and the CANDELS GOODS-S field compared to our previous analysis in Oesch et al. (2012a), we are able to improve our constraints on the $z \sim 10$ LF.

These new constraints at $z \sim 9\text{--}11$ will allow us to test whether the galaxy population underwent accelerated evolution at $z > 8$ as previously found in Bouwens et al. (2011a) and Oesch et al. (2012a), or whether the UV LF trends from lower redshift continue unchanged to $z > 8$ (the preferred

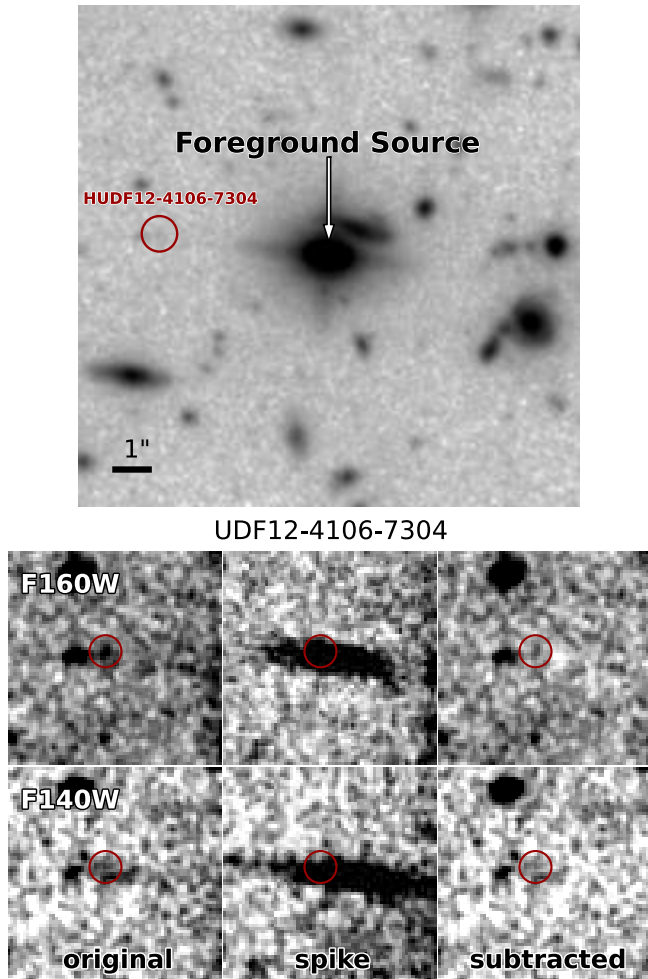


Figure 9. The flux of the $z \sim 9.5$ candidate HUDF12-4106-7304 of Ellis et al. (2013) appears to be significantly boosted by a diffraction spike. Top: a $15''$ view around the bright foreground neighbor of the source HUDF12-4106-7304. The source clearly lies exactly along the direction of the diffraction spike caused by the bright neighbor. Bottom: stamps ($4''$ by $4''$) of the $z \sim 9.5$ candidate HUDF12-4106-7304 of Ellis et al. (2013) (left) next to an image of a diffraction spike of a nearby star (center), with the rescaled flux of the diffraction spike subtracted from the UDF12-4106-7304 image (right). The latter was derived by fitting the core of the bright galaxy to the right (west) of HUDF12-4106-7304. This was done for both F140W and F160W. The images are centered at the same pixel offset from the nearby bright object causing the diffraction spike. The bright object lies 5 arcsec to the right (W) in each case. The location of the putative $z \sim 9.5$ candidate is marked as a red circle. It clearly lies extremely close to where the peak flux of the diffraction spike is expected. A hint of a linear spike is seen in the JH_{140} image, running across the source location. While a source is still seen in the subtracted image, its estimated flux is reduced by a factor ~ 2 , making this a 2.8σ detection only. This very weak detection evidence, together with the near blending of the source with another foreground galaxy, strongly suggests that this is not a real source. Such faint higher-order diffraction spikes are a well-known pitfall when pushing the data to their limits, in particular in ultra-deep imaging data, which are mostly taken at the same rotation angle.

(A color version of this figure is available in the online journal.)

interpretation of, e.g., Ellis et al. 2013; Coe et al. 2013; Zheng et al. 2012).

In order to test for such accelerated evolution, we start by estimating the number of galaxies we would have expected to see in our $z \sim 9$ –11 LBG samples, if the lower-redshift trends were to hold unchanged at $z > 8$. By comparing the observed number of sources with those expected from the extrapolations,

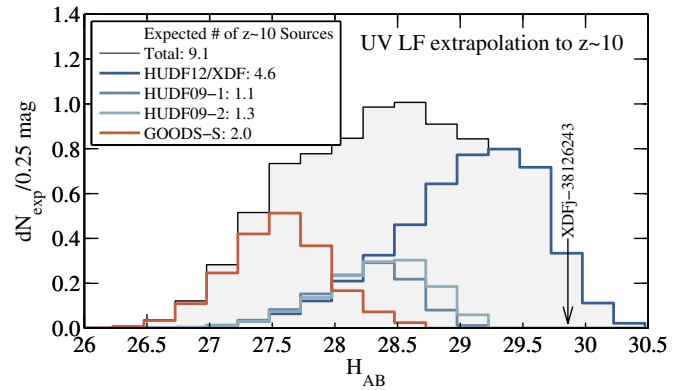


Figure 10. Expected number of $z \sim 10$ candidates per bin of 0.25 mag in the different fields considered in our analysis, assuming that the UV LF evolves steadily from $z \sim 8$ to $z \sim 10$, consistent with the well-established trends from $z \sim 8$ to $z \sim 4$. With this assumption the HUDF12/XDF alone should have contained 4.6 candidate galaxies at $z \sim 10$. In our whole survey area, we would have expected to see ~ 9 sources now. Given that only one candidate galaxy could be identified (shown by the arrow), this provides strong, direct evidence that the UV luminosity function and LD are evolving rapidly from $z \sim 10$ to $z \sim 8$.

(A color version of this figure is available in the online journal.)

we derive a direct estimate of any changes in the evolution of galaxies at $z > 8$.

To derive the expected numbers, we use our estimates of the selection function and completeness measurements described in Section 3.6. This allows us to compute the number of sources expected as a function of observed magnitude. For an assumed LF $\phi(M)$, this is given by

$$N_i^{\text{exp}} = \int_{\Delta m} dm \int dz \frac{dV}{dz} S(m, z) C(m) \phi(M[m, z]). \quad (5)$$

For the UV LF evolution, we adopt the relations of Bouwens et al. (2011b): $\phi_* = 1.14 \times 10^{-3} \text{ Mpc}^{-3} \text{ mag}^{-1} = \text{const}$, $\alpha = -1.73 = \text{const}$, and $M_*(z) = -20.29 + 0.33 \times (z - 6)$. Note that we assume constant values for the faint-end slope α and the normalization ϕ_* . These relations are used as a baseline, when extrapolated to higher redshifts, to test whether the observed galaxy population at $z > 8$ is consistent with the trends at later times, i.e., at lower redshifts.

With these assumptions, we find that we would expect to detect a total of 17 ± 4 galaxies in our $z \sim 9$ YJ-dropout sample over the HUDF12/XDF field alone. Yet, after correcting for one potential contaminant (see Section 3.5.2), we only detect six sources. This is $2.8\times$ fewer than expected from the trends from the lower-redshift LFs.

Similarly, with the same assumptions about the evolution of the UV LF from $z \sim 4$ to $z \sim 10$, we would expect to see a total of 9 ± 3 sources in our $z \sim 10$ J-dropout sample. We only find one such source, which suggests that beyond $z \sim 9$, the decrement compared to the baseline evolution is even larger than we found previously from the HUDF09 and the six-epoch CANDELS data. We now expect to see three more sources compared to the six that we expected to see in the earlier analysis of Oesch et al. (2012a). Yet, no additional $z \sim 10$ sources are found.

The expected magnitude distribution for the $z \sim 10$ sample is shown in Figure 10. As indicated in the figure, our search for $z \sim 10$ sources in the CANDELS and ERS fields of GOODS-S should have resulted in two detections. Only 0.5 sources were

Table 3
Summary and Comparison of $z \gtrsim 8.5$ LF Determinations in the Literature

Reference	Redshift	$\log \phi_*$ ($\text{Mpc}^{-3} \text{ mag}^{-1}$)	M_{UV}^* (mag)	α
This work	11	-2.94 (fixed)	> -18.4 (1σ)	-1.73 (fixed)
This work	10	-2.94 (fixed)	-17.7 ± 0.7	-1.73 (fixed)
This work	9	-2.94 (fixed)	-18.8 ± 0.3	-1.73 (fixed)
Oesch et al. (2012a)	10	-2.96 (fixed)	-18.0 ± 0.5	-1.74 (fixed)
Bouwens et al. (2012a)	9.2	-3.96 ± 0.48	-20.04 (fixed)	-2.06 (fixed)

expected in these fields from our previous analysis using somewhat shallower data (Oesch et al. 2012a).

Depending on the assumptions about halo occupation, the expected cosmic variance for a single WFC3/IR field is 40%–45% (Trenti & Stiavelli 2008; Robertson 2010). In order to estimate the significance of our finding of a large offset (i.e., decrement) between the expected number of sources and that seen, we have to combine the Poissonian and cosmic variance uncertainties. We estimate the chance of finding ≤ 1 source in our full search area using the appropriate expected number counts and cosmic variance estimates for the individual search fields. The latter are based on the cosmic variance calculator of Trenti & Stiavelli (2008). Using simple Monte Carlo simulations, we derive that given that we expected to find nine sources, finding ≤ 1 occurs at a probability of only 0.5%. Therefore, our data are inconsistent with a simple extrapolation of the lower-redshift LF evolution at 99.5%.

This new estimate reinforces the conclusion of Bouwens et al. (2011a) and Oesch et al. (2012a) that the evolution in the number density of star-forming galaxies between $z \sim 10$ and $z \sim 8$ is large, and larger than expected from the rate of increase at later times, i.e., the evolution was accelerated in the ~ 200 Myr from $z \sim 10$ to $z \sim 8$.

4.2. The UV Luminosity Function at $z > 8$

The above calculations of the expected number of sources can be used directly to constrain the UV LFs at $z \sim 9$ –11. Since the number of candidates is small, we need to make some assumptions about how to characterize the evolution. The UV LFs at later times provide a valuable guide. The parameter that evolves the most is the characteristic luminosity L_* ; the normalization (ϕ_*) and the faint-end slope (α) are relatively unchanged from $z \sim 8$ to $z \sim 4$ (although we do have evidence for evolution toward steeper faint-end slopes). This suggests that we should estimate what evolution in the characteristic luminosity best reproduces the observed number of sources, while keeping both the normalization and the faint-end slope fixed.

Doing so results in a best estimate of the luminosity evolution of $dM/dz = 0.49 \pm 0.09$ from $z \sim 6$ to $z \sim 9$ and $dM/dz = 0.6 \pm 0.2$ to $z \sim 10$. The characteristic magnitudes at these redshifts are thus expected to be $M_*(z \sim 9) = -18.8 \pm 0.3$ and $M_*(z \sim 10) = -17.7 \pm 0.7$. The uncertainties on these measurements are still quite large, given the small sample sizes and the small area probed, in particular for the $z \sim 9$ search.

We perform the same calculation for the $z \sim 10.7$ JH₁₄₀-dropout sample. However, given the uncertain nature of the single candidate source in that sample (XDFjh-39546284), we treat the estimate at $z \sim 10.7$ as an upper limit. We therefore compute the evolution in M_* which is needed to produce one source or fewer in the sample. This is found to be $dM/dz > 0.4$, which is a less stringent constraint than that for our $z \sim 10$

Table 4
Step-wise Determination of the $z \sim 9$ and $z \sim 10$ UV LF Based on the Present Dataset

M_{UV} (mag)	ϕ_* ($10^{-3} \text{ Mpc}^{-3} \text{ mag}^{-1}$)
$z \sim 9$	
-20.66	< 0.18
-19.66	$0.15^{+0.15}_{-0.13}$
-18.66	$0.35^{+0.24}_{-0.24}$
-17.66	$1.6^{+0.9}_{-0.9}$
$z \sim 10$	
-20.78	$< 0.0077^a$
-20.28	< 0.013
-19.78	< 0.027
-19.28	< 0.083
-18.78	< 0.17
-18.28	< 0.34
-17.78	$0.58^{+0.58}_{-0.50}$

Note. ^a 1σ upper limit for a non-detection.

estimate, due to the much smaller area probed by our $z \sim 10.7$ search. The inferred constraint on the characteristic magnitude is $M_*(z = 10.7) > -18.4$ mag. All our estimates of the UV LFs are summarized in Table 3.

The above estimates for the characteristic luminosity of the UV LF can also be compared with the characteristic luminosity from the step-wise determination of the LF using the observed galaxies and limits. The step-wise LF is derived using an approximation of the effective selection volume as a function of observed magnitude $V_{\text{eff}}(m) = \int_0^\infty dz (dV/dz) S(z, m) C(m)$. The LF is then simply $\phi(M_i) dM = N_i^{\text{obs}} / V_{\text{eff}}(m_i)$. Errorbars on the step-wise LF measurements are computed based on Poissonian statistics, with an addition of 45% cosmic variance uncertainty for a single WFC3/IR pointing (Trenti & Stiavelli 2008).

The above approximation of the effective volume is only valid as long as the absolute magnitude varies slowly with observed magnitude. This is not the case for $z > 11$, since the IGM absorption affects the H_{160} band such that the relation between luminosity and the observed magnitude becomes strongly redshift dependent. We therefore restrict our analysis of the step-wise LFs to the $z < 10.7$ samples. In any case, the small area probed by the HUDF12/XDF data currently does not significantly constrain the UV LF at $z \sim 11$. The step-wise $z \sim 9$ and $z \sim 10$ LFs are tabulated in Table 4.

Figure 11 shows our constraints on the UV LF at $z \sim 9$ and $z \sim 10$. The expected UV LFs extrapolated from the lower-redshift trends are shown as dashed lines. Clearly, at both redshifts, the observed LF lies significantly below this

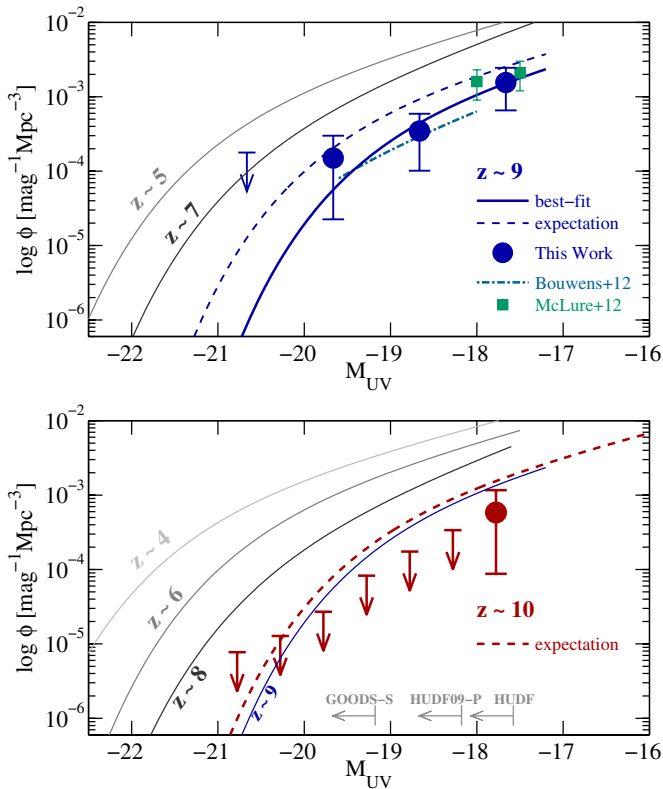


Figure 11. Constraints on the $z \sim 9$ (top) and $z \sim 10$ (bottom) UV LF from the HUDF12/XDF data as well as from the additional fields for $z \sim 10$. Lower-redshift LFs are shown as gray solid lines for illustration of the LF evolution trends. These are the most recent determinations from Bouwens et al. (2007, 2012b) at $z = 4-7$ and Oesch et al. (2012b) at $z \sim 8$. Top: our step-wise $z \sim 9$ LF (dark blue circles) is computed in bins of 1 mag, which contain one, two, and three sources, respectively. These measurements are consistent with (but consistently below) the expected LF given an extrapolation from lower redshift (dashed blue line). The best-fit LF based on luminosity evolution is shown as a solid blue line. This is derived from the expected number of sources in bins 1 mag wide, and is a factor $\sim 1.5-4\times$ below the extrapolated LF. Also shown as green squares is the step-wise $z \sim 9$ determination from McLure et al. (2013), who use a photometric redshift sample derived from HUDF12 data. Their determination is in very good agreement with our measurement, although it is unclear why they only constrain the LF at the very faint end. The dot-dashed line represents the best $z \sim 9$ LF estimate of Bouwens et al. (2012a) over the magnitude range where it is constrained by their lensed candidates from the CLASH dataset. Their determination is based on scaling the normalization of the $z \sim 8$ LF to account for the low number density of $z \sim 9$ LBG candidates found over the first 19 clusters. Within the current uncertainties, all three determinations of the $z \sim 9$ LFs are in good agreement, finding accelerated evolution compared to the lower-redshift trends. Bottom: at $z \sim 10$, our analysis includes several additional fields, which is why we can probe to much lower volume densities than for our $z \sim 9$ LF. Nevertheless, since we only find one potential $z \sim 10$ galaxy candidate in our data, we can mostly only infer upper limits on the LF. Again, these are consistently below the extrapolated LF (dashed red line), indicating that the galaxy population evolves more rapidly at $z > 8$ than at lower redshift.

(A color version of this figure is available in the online journal.)

extrapolation, as expected from our analysis of the observed number of sources in the previous section.

The best-fit $z \sim 9$ LF using M_* evolution is a factor $1.5-5\times$ below the extrapolated LF at $M_{UV} > -20$ mag. At the bright end, the small area probed by the single HUDF12/XDF field limits our LF constraints to $\gtrsim 10^{-4} \text{ mag}^{-1} \text{ Mpc}^{-3}$, which is clearly too high to be meaningful at $M_{UV} < -20$. It will therefore be very important to cover several fields with F140W imaging in the future in order to push the $z \sim 9$ selection volumes to interesting limits.

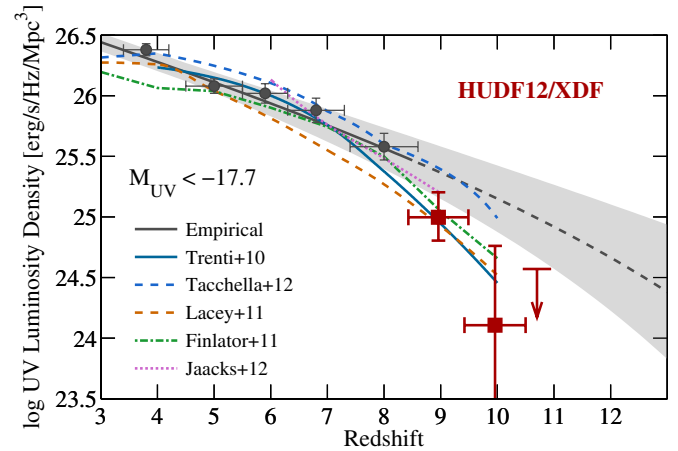


Figure 12. The evolution of the UV luminosity density (LD) ρ_{UV} contributed by all galaxies brighter than $M_{1400} = -17.7$ mag. Our new measurements from the HUDF12/XDF data are shown as red squares. Measurements of the LD at $z \leq 8$ are derived from the UV LFs from Bouwens et al. (2007, 2012b). No correction for dust extinction has been applied. The measurements are plotted at the mode of the redshift distributions shown in Figure 6. For the highest-redshift $z \sim 10.7$ JH-dropout sample, we only show an upper limit given that the single source we find in this sample is either at an even higher redshift (where the selection volume of our data is very small) or is a low-redshift extreme line emitter. The dark gray line and shaded area represent an extrapolation of the redshift evolution trends of the $z \sim 4-8$ UV LF. Our LD estimates at $z \sim 9-10$ are clearly lower than this extrapolation. However, the observed rapid build-up of galaxies at $z \sim 10$ to $z \sim 8$ is not unexpected, since it is consistent with a whole suite of theoretical models. Some of these are shown as colored lines. They are halo occupation models (blue solid and dashed; Trenti et al. 2010; Tacchella et al. 2013), a semi-analytical model (orange dashes; Lacey et al. 2011), and two hydrodynamical simulations (Finlator et al. 2011; Jaacks et al. 2012). These different models uniformly predict a steepening in the LD evolution at $z > 8$. The conclusion to be drawn is that the shape of the trend from $z \sim 10$ to $z \sim 7$ is mainly due to the rapid build-up of the underlying dark matter halo mass function, rather than any physical changes in the star formation properties of galaxies.

(A color version of this figure is available in the online journal.)

At $z \sim 10$, the use of deeper data both on the HUDF and on the GOODS-S field allows us to push our previous constraints on the UV LF to fainter limits. Since we only detect one $z \sim 10$ galaxy candidate, however, our constraints mainly consist of upper limits. Nevertheless, it is evident that at all magnitudes $M_{UV} > -20$ mag these upper limits are consistently below the extrapolated UV LF, up to a factor $4\times$ lower. Additionally, the limits are also clearly below the best-fit $z \sim 9$ LF, showing that the UV LF continues to decline at $z > 9$.

4.3. The UV Luminosity Density Evolution at $z > 8$

The evolution of the UV LD at $z > 8$ has received considerable attention in recent papers, triggered by our initial finding of a significant drop in the LD from $z \sim 8$ to $z \sim 10$ (i.e., a rapid increase in the LD within a short period of time). With the new HUDF12/XDF data, it is now possible to refine this measurement by adding a $z \sim 9$ and a $z \sim 11$ point, while also allowing us to improve upon our previous measurements at $z \sim 10$.

The UV LDs inferred from our $z > 8$ galaxy samples are shown in Figure 12. The measurements show the LD derived by integrating the best-fit UV LF determined in the previous section. The integration limit is set to $M_{UV} = -17.7$ mag, which is the current limit probed by the HUDF12/XDF data. For comparison, we also show the lower-redshift LD measurements from the compilation of Bouwens et al. (2007, 2012d). These

Table 5

Summary of Luminosity Density and Star Formation Rate Density Estimates

Dropout Sample	Redshift	$\log_{10} \rho_{UV}^a$ ($\text{erg s}^{-1} \text{Hz}^{-1} \text{Mpc}^{-3}$)	$\log_{10} \rho_*$ ($M_{\odot} \text{yr}^{-1} \text{Mpc}^{-3}$)
<i>YJ</i>	9.0	$25.00^{+0.19}_{-0.21}$	$-2.86^{+0.19}_{-0.21}$
<i>J</i>	10.0	$24.1^{+0.7}_{-0.9}$	$-3.7^{+0.7}_{-0.9}$
<i>JH</i>	10.7	<24.6	<-3.3
<i>B</i>	3.8	26.38 ± 0.05	-1.21 ± 0.05
<i>V</i>	5.0	26.08 ± 0.06	-1.54 ± 0.06
<i>i</i>	5.9	26.02 ± 0.08	-1.72 ± 0.08
<i>z</i>	6.8	25.88 ± 0.10	-1.90 ± 0.10
<i>Y</i>	8.0	25.58 ± 0.11	-2.20 ± 0.11

Notes. The lower-redshift data points are based on the UV LFs from Bouwens et al. (2007, 2011b) and Oesch et al. (2012b).

^a Integrated down to $0.05 L_{z=3}^*$ ($M_{1400} = -17.7$ mag).

were computed in the same manner as the new $z > 8$ values, and were not corrected for dust extinction. A summary of our measurements for the LD is listed in Table 5.

As can be seen, our new measurements at $z > 8$ lie significantly below the $z \sim 8$ value. The decrement in LD from $z \sim 8$ to $z \sim 9$ is 0.6 ± 0.2 dex, and it is even larger at 1.5 ± 0.7 dex to $z \sim 10$. Therefore, our data confirm our previous finding of more than an order of magnitude increase of the UV LD in the short time period, only 170 Myr, from $z \sim 10$ to $z \sim 8$.

The gray line and shaded area show the expected LD evolution when extrapolating the $z \sim 4-8$ Schechter function trends to higher redshift. All our measurements at $z > 8$ lie below the extrapolation. Although the offsets individually are not large (they are $<2\sigma$), the consistent offset to lower LD supports a hypothesis that significant changes are occurring in the LD evolution at $z > 8$.

It is interesting to note that this offset to lower LD is not unexpected, as it is also seen in several theoretical models. In Figure 12, we compare our observational results to two conditional LF models from Trenti et al. (2010) and Tacchella et al. (2013), the prediction from a semi-analytical model of Lacey et al. (2011), as well as the results from two hydrodynamical simulations of Finlator et al. (2011) and Jaacks et al. (2012).

All these models are in relatively good agreement with the lower-redshift ($z < 8$) measurements. As can be seen from the figure, essentially all models do show a steeper evolution at $z > 8$ than a purely empirical extrapolation of the UV LF further into the epoch of reionization. Since these models are all very different in nature, this strongly suggests that the rapid build-up we observe in the galaxy population is mainly driven by the build-up in the underlying dark matter halo mass function, which is also evolving very rapidly at these epochs.

4.4. The SFRD Build-up from $z \sim 11$ to $z \sim 8$

Our results combined with those of others now provide a substantially larger sample at $z \gtrsim 8$ for estimate of the SFRD than was available for Bouwens et al. (2011a) and Oesch et al. (2012a). The SFRD at $z > 8$ was recently estimated based on four high-redshift galaxies identified in the CLASH survey (Bouwens et al. 2012a; Coe et al. 2013; Zheng et al. 2012), and from seven galaxies identified in the HUDF12 data (Ellis et al. 2013). We present all these results, together with our own measurements in Figure 13, where we plot the SFRD as a function of redshift in star-forming galaxies with

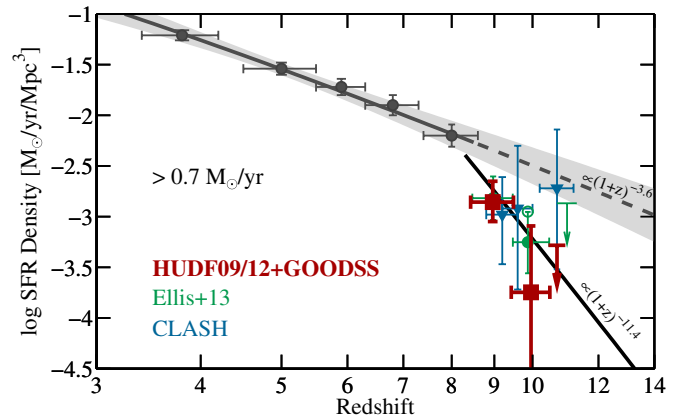


Figure 13. The evolution of the star formation rate density (SFRD) $\dot{\rho}_*$ contributed by star-forming galaxies brighter than $M_{1400} = -17.7$ mag. This limit corresponds to a star formation limit $>0.7 M_{\odot} \text{yr}^{-1}$. Measurements at $z > 8$ are shown from the present analysis (dark red squares), from the HUDF12 analysis of Ellis et al. (2013, green circles), as well as from CLASH cluster detections (blue triangles; Bouwens et al. 2012a; Coe et al. 2013; Zheng et al. 2012). The lower-redshift datapoints are derived from UV LFs from Bouwens et al. (2007, 2012b). The SFRD is derived from the UV LD integrated to these limits and corrected for dust extinction using the most recent estimates from Bouwens et al. (2012c). A clear decrement by 0.6 dex in the SFRD is consistently seen between the measurement at $z \sim 8$ and that at $z \sim 9$. At redshifts higher than $z \sim 9$, all datapoints only contain one galaxy, resulting in large uncertainties. (We have corrected down the measurement of Ellis et al. to account for a likely diffraction spike source; cf. open vs. filled green circle at $z \sim 10$.) Given the large uncertainties, the individual $z > 8$ measurements are all consistent with each other. At $z = 4-8$ the SFRD increases gradually, following $\dot{\rho}_* \propto (1+z)^{-3.6 \pm 0.3}$ (dark gray line). The extrapolation of this trend to higher redshift is shown by the dashed line and gray region (1σ). All data points lie below this line, indicating that the extrapolation is not a good fit. The combined best-fit evolution using all the CLASH measurements and our new HUDF12/XDF results is significantly steeper, following $(1+z)^{-11.4 \pm 3.1}$ (black solid line). The Ellis et al. (2013) datapoints were excluded from this fit due to overlap in the adopted data with our work. While we find an increase by a factor $30\times$ in the SFRD between $z \sim 10$ and $z \sim 8$ from our HUDF12+GOODSS analysis alone, the best-fit trend results in a somewhat reduced increase. Nevertheless, this is still a factor $10\times$ in the ~ 170 Myr from $z \sim 10$ to $z \sim 8$, i.e., a large change over a short time period.

(A color version of this figure is available in the online journal.)

SFR $> 0.7 M_{\odot} \text{yr}^{-1}$ (corresponding to a magnitude limit of $M_{UV} = -17.7$ mag).

The SFRDs are derived from the UV LD estimates after correction for dust extinction. We use the most recent determinations of the UV continuum slopes β as a function of UV luminosity and redshift from Bouwens et al. (2012c) together with the Meurer et al. (1999) β -extinction relation. The dust-corrected LDs are then converted to SFRDs using the conversion factor of Madau et al. (1998), assuming a Salpeter initial mass function.

Across $z \sim 4$ to $z \sim 8$, the SFRD clearly evolves very uniformly. The evolution is well reproduced by a power law $\dot{\rho}_* \propto (1+z)^{-3.6 \pm 0.3}$, which is shown as a dark gray line in Figure 13. Interestingly, all measurements lie below the extrapolation of this trend to higher redshift. Again, individual measurements are within $<2\sigma$ of the trend, but the offset to smaller SFRDs in the mean is very clear.

Note that each of the three groups finds a consistent decrement of the SFRD from $z \sim 8$ to $z \sim 9$. Specifically, from our data, we find a drop by 0.6 ± 0.2 dex. This is $\sim 2\sigma$ below the simple extrapolation of the lower-redshift trends.

At $z \sim 9$ our SFRD estimate is in excellent agreement with the measurement of Ellis et al. (2013) based on a photometric redshift selection. At $z \sim 10$, however, we find a significantly

lower value, mainly due to our inclusion of a larger dataset covering a larger area, in which we do not find any additional candidate. Nevertheless, our measurement is within $\sim 1\sigma$ of the result of Ellis et al. (2013), in particular, after we correct their measurement down by a factor two to account for the source that is likely the result of a diffraction spike in their $z = 9.5$ sample (Figure 9).

Also at $z \sim 10.7$, our upper limit is significantly below the $z = 11$ estimate of Ellis et al. (2013). This is likely due to the wide redshift range probed by our JH_{140} -dropout sample, which extends from $z \sim 9.5$ to $z \sim 11.8$ (see Figure 8). Ellis et al. (2013) consider a strict boundary of $z = 10.5$ to $z = 11.5$.

It is interesting to derive a best-fit evolution of the SFRD at $z \geq 8$ which includes all the current datasets available. We do this by combining all $z > 8$ measurements from CLASH with our improved estimates at $z \sim 9$ – 11 , together with the previous $z \sim 8$ SFRD measurement (Oesch et al. 2012b). The results of Ellis et al. (2013) are not included due to significant overlap with our dataset here.

The resulting best-fit evolution of the SFRD falls off very rapidly, following $\dot{\rho}_* \propto (1+z)^{-11.4 \pm 3.1}$. This is shown as the black line in Figure 13. As can be seen, this is significantly steeper than the $z \sim 4$ – 8 trends. By $z \sim 10$, the best-fit evolution is already a factor $\sim 5\times$ below the lower-redshift trend. Therefore, the combined constraint on the SFRD evolution from all datasets in the literature clearly points to an accelerated evolution at $z > 8$.

5. SUMMARY AND CONCLUSIONS

We have used the new, ultra-deep WFC3/IR data over the HUDF field as well as the optical XDF data to provide a reliable selection of galaxies at $z > 8$. The new observations from the HUDF12 program push the depth of the H_{160} imaging deeper by ~ 0.2 mag compared to our previous data from the HUDF09 survey, and they provide additional JH_{140} imaging. The JH_{140} data are very useful for selecting some of the first $z \sim 9$ and $z \sim 11$ galaxy samples using the Lyman break technique. Furthermore, we extended our previous search for $z \sim 10$ galaxies (Oesch et al. 2012a) to fainter limits by including this new HUDF12/XDF data set. Our analysis is the most extensive search for $z > 8$ galaxies to date.

From our full dataset, we find a total sample of nine $z > 8$ galaxy candidates. Seven of these lie in our $z \sim 9$ selection. Contamination is always a central concern for high-redshift samples, and after careful analysis we expect that the contamination fraction is small, being only about 15%–20%.

We found that one of the $z \sim 9$ sources has a very wide photometric redshift likelihood distribution, with an ambiguous best fit at $z_{\text{phot}} = 2.2$ (using ZEBRA; $z_{\text{phot}} = 8.6$ using EAZY). We therefore exclude this source from the subsequent analysis.

We discover a new $z \sim 10$ source (at $z = 9.8 \pm 0.6$), making it one of the very few galaxies known at this very high redshift, just 460 Myr after the big bang. The highest-redshift candidate in our sample is XDFjh-39546284 that was previously identified at $z \sim 10.4$. However, these new data (the JH_{140} in particular) constrain this galaxy to be at $z \sim 11.8$, if it is at high redshift. This interpretation is problematic and has led to discussion about it being a possible lower-redshift $z \sim 2$ object, and so its true nature remains quite uncertain at this time (see Ellis et al. 2013; Bouwens et al. 2012d; Brammer et al. 2013).

Our sample selection of $z > 8$ galaxy candidates is in good agreement with the previous analysis of Ellis et al. (2013) and McLure et al. (2013), who performed a photometric redshift

selection of $z > 8.5$ sources over the HUDF12 field only. Five out of our six $z \sim 9$ candidates are also selected in the McLure et al. (2013) catalogs. Conversely, our selection includes all of the $z > 8.5$ candidates presented in Ellis et al. (2013), with the exception of two sources. One of these is most likely contaminated by a diffraction spike of a nearby bright source (see Figure 9), while the other one has low S/N and lands just outside of our color selection box. The consistency of these two sample selections is very reassuring and raises the confidence in both the color and the photometric redshift selections of $z > 8$ galaxy candidates.

Our sample of $z > 8$ galaxy candidates proves to be very important for setting a number of constraints on galaxy build-up at very early times, allowing us to derive one of the first estimates of the UV LF at $z \sim 9$, to improve our constraints at $z \sim 10$, and to set limits at $z \sim 11$.

The main result from our analysis is a confirmation of our previous finding that the galaxy population, as seen down to $M_{\text{UV}} = -17.7$ mag, evolves much more rapidly at $z > 8$ than at lower redshift (identified as “accelerated evolution”; Bouwens et al. 2011a; Oesch et al. 2012a). This is seen in (1) the expected number of galaxies when extrapolating the lower-redshift trends to $z > 8$ (Figure 10), (2) the direct constraints on the UV LF (Figure 11), and (3) the evolution of the luminosity and SFRDs down to our current completeness limits (Figures 12 and 13). All measurements consistently point to accelerated evolution at early times, beyond $z \sim 8$.

Specifically, if the lower-redshift trends of the UV LF are extrapolated to $z \sim 10$, we would have expected to see 9 ± 3 candidate sources in our full data set, ~ 5 of which only in the HUDF12/XDF data alone. However, only one such candidate is found in the HUDF12/XDF data, which suggests that the galaxy population evolves more rapidly than at lower redshift at 99.5% significance (see Section 4.1).

From $z \sim 8$ to $z \sim 9$, the LD in star-forming galaxies with $\text{SFR} > 0.7 M_{\odot} \text{ yr}^{-1}$ (i.e., $M_{\text{UV}} < -17.7$) decreases by 0.6 ± 0.2 dex. This decrement is fully consistent with previous estimates from CLASH (Bouwens et al. 2012a) and from the HUDF12 data alone (Ellis et al. 2013).

The combination of our new measurements of the SFRD at $z > 8$ with all previous estimates from the CLASH data (Bouwens et al. 2012a; Coe et al. 2013; Zheng et al. 2012) results in a best-fit evolution which is extremely steep, following $\dot{\rho}_* \propto (1+z)^{-11.4 \pm 3.1}$.

These results on the galaxy evolution at $z > 8$ contrast with the conclusions drawn by several recent papers, who argue that the UV LD evolution at $z > 8$ is consistent with the lower-redshift trends (e.g., Ellis et al. 2013; Coe et al. 2013; Zheng et al. 2012). However, the small sample sizes of $z > 8$ galaxies in these individual analyses resulted in large uncertainties on the LD and SFRD evolution. We show here that once all these measurements are combined self-consistently, they do indeed point to accelerated evolution at $z > 8$, consistent with theoretical expectations.

Note that the steep fall-off we find in the UV LD at $z > 8$ is not at odds with galaxies driving reionization. Our measurements only reach to $\sim L^*$ at $z \sim 10$ (i.e., to $M_{\text{UV}} = -17.7$ mag). However, with the steep faint-end slopes that are consistently found for $z > 4$ UV LFs, the total LD is completely dominated by galaxies below this threshold (see, e.g., Bouwens et al. 2012b; Kuhlen & Faucher-Giguère 2012).

With WFC3/IR we are now in a similar situation in studying $z \sim 9.5$ – 10 as we were three years ago with NICMOS at $z \sim 7$.

Galaxy samples are still small, and the conclusions are uncertain. However, over the next few years the $z > 8$ frontier will be explored more extensively. In particular, the additional deep field observations to be taken as part of the Frontier Fields Initiative (a large Director's Discretionary program) will significantly increase sample sizes and should allow for improved constraints on the $z \sim 9$ and $z \sim 10$ LF at $M_{UV} < -18.5$ mag. This will enable more precise constraints on the accelerated evolution that we now see in the galaxy population from the data over GOODS-South.

We thank the anonymous referee for very constructive comments to improve our paper. Support for this work was provided by NASA through Hubble Fellowship Grant HF-51278.01 awarded by the Space Telescope Science Institute, which is operated by the Association of Universities for Research in Astronomy, Inc., for NASA, under contract NAS 5-26555.

Additionally, this work has been supported by NASA Grants NAG5-7697 and HST-GO-11563.01.

Facilities: *HST* (ACS/WFC3), *Spitzer* (IRAC).

APPENDIX

MAGNITUDE-DEPENDENT REDSHIFT SELECTION FUNCTIONS

The main advantage of an LBG analysis over a photometric redshift selection is that the selection volume and expected redshift distributions as a function of luminosity can be estimated in a rather straightforward manner through simulations. As discussed in the main text, this is done by inserting artificial galaxies into the science images and rerunning the selection procedure exactly as for the real observations.

In Figure 8, we have presented the redshift selection functions that we derived for the three LBG selections used in this paper. Here, we additionally show how these selection functions

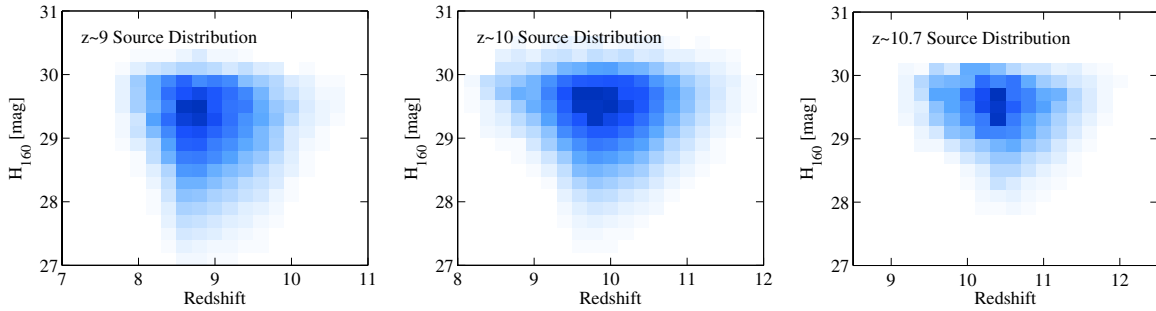


Figure 14. The expected magnitude and redshift distributions for the three different LBG selections applied to the XDF dataset. Effectively, we plot the expected number of candidates per bin of redshift and H_{160} magnitude given the UV LF prior (see also Equation (4)). These three panels are the two-dimensional version of Figure 8, where we marginalized over magnitude to only show the redshift selection. However, the redshift distributions of these LBG selections are strongly magnitude dependent as can be seen in all three panels above. This is due to larger photometric scatter at fainter magnitudes, which causes sources to land in the color selection box over a somewhat wider redshift range than at bright magnitudes. The peak in the magnitude distribution of the sample is determined by the specific Schechter function parameters and the magnitude-dependent completeness.

(A color version of this figure is available in the online journal.)

Table 6
Photometry of Additional Potential $z > 8$ LBG Candidates Not Used in This Analysis

ID	R.A. z_{EBRA} z_{phot}	Decl. z_{EAZY} z_{phot}	H_{160}	$(YJ) - JH_{140}$	$J_{125} - H_{160}$	$JH_{140} - H_{160}$	$S/N_{H_{160}}$	$S/N_{JH_{140}}$	$S/N_{J_{125}}$	χ^2_{opt}
42126501	03:32:42.12 $9.5^{+0.1}_{-0.1}$	-27:46:50.1 $9.7^{+0.1}_{-0.2}$	28.45 ± 0.05	1.7 ± 0.2	1.4 ± 0.2	0.3 ± 0.1	22.2	15.8	5.2	-0.1
This potential source is completely blended with a foreground galaxy.										
43246481	03:32:43.24 $2.5^{+6.1}_{-0.7}$	-27:46:48.1 $2.4^{+7.7}_{-0.4}$	28.61 ± 0.17	0.8 ± 0.6	1.3 ± 0.7	0.7 ± 0.4	5.4	3.0	2.8	-1.9
Close to bright, clumpy foreground galaxy.										
43286481	03:32:43.28 $10.4^{+0.5}_{-0.5}$	-27:46:48.1 $10.6^{+0.6}_{-0.3}$	28.53 ± 0.17	> 1.6	> 1.9	0.8 ± 0.4	6.0	2.5	0.5	-0.2
Close to bright, clumpy foreground galaxy.										
Additional sources from Ellis et al. (2013)										
UDF12-4106-7304	03:32:41.06 ...	-27:47:30.4
The photometry of this source is significantly affected by a diffraction spike (see Figure 9).										
After subtraction of the expected flux of the spike, the source is only a 2.8σ total NIR detection.										
UDF12-3895-7115	03:32:38.95 $0.5^{+5.8}_{-0.5}$	-27:47:11.5 $0.6^{+8.2}_{-0.5}$	30.02 ± 0.30	0.5 ± 0.5	0.1 ± 0.5	0.1 ± 0.5	3.5	3.7	3.7	1.2
Does not satisfy our color selection: $(YJ) - JH_{140} = 0.5 < 0.75$.										
Additionally, the best-fit photometric redshift is only 0.5 using our photometry.										
Additional previous $z \gtrsim 8$ candidates from Bouwens et al. (2011a)										
UDFy-37806001	03:32:37.80 $7.8^{+0.2}_{-0.4}$	-27:46:00.1 $7.9^{+0.3}_{-0.4}$	28.39 ± 0.12	0.4 ± 0.1	-0.2 ± 0.2	-0.2 ± 0.1	10.1	13.7	9.4	2.7
Too blue in $(YJ) - JH_{140}$ for our selection.										
UDFy-33446598	03:32:33.44 $7.7^{+0.4}_{-0.4}$	-27:46:59.8 $7.7^{+0.5}_{-0.4}$	29.00 ± 0.20	0.3 ± 0.2	0.1 ± 0.3	0.1 ± 0.2	5.6	6.0	4.7	-1.9
Too blue in $(YJ) - JH_{140}$ for our selection.										

Note. S/N are measured in circular apertures of fixed $0''.35$ diameter.

depend on magnitude as well. In Figure 14, we show the relative magnitude and redshift distributions of our samples in the XDF data based on our simulations. Specifically, we plot the expected number of sources in a bin of redshift and magnitude given a prior UV LF (see also Section 3.6). As can be seen from the figure, the redshift distributions are quite sensitive to the magnitude of the sources. This is solely due to larger photometric scatter which causes fainter sources to be selected in our color-color diagrams over a wider redshift range.

REFERENCES

- Beckwith, S. V. W., Stiavelli, M., Koekemoer, A. M., et al. 2006, *AJ*, **132**, 1729
- Bertin, E., & Arnouts, S. 1996, *A&AS*, **117**, 393
- Bouwens, R., Bradley, L., Zitrin, A., et al. 2012a, arXiv:1211.2230
- Bouwens, R., Broadhurst, T., & Illingworth, G. 2003, *ApJ*, **593**, 640
- Bouwens, R. J., Illingworth, G. D., Blakeslee, J. P., Broadhurst, T. J., & Franx, M. 2004, *ApJL*, **611**, L1
- Bouwens, R. J., Illingworth, G. D., Franx, M., & Ford, H. 2007, *ApJ*, **670**, 928
- Bouwens, R. J., Illingworth, G. D., Franx, M., et al. 2009, *ApJ*, **705**, 936
- Bouwens, R. J., Illingworth, G. D., Labbe, I., et al. 2011a, *Natur*, **469**, 504
- Bouwens, R. J., Illingworth, G. D., Labbe, I., et al. 2011b, *ApJ*, **737**, 90
- Bouwens, R. J., Illingworth, G. D., Oesch, P. A., et al. 2010, *ApJL*, **708**, L69
- Bouwens, R. J., Illingworth, G. D., Oesch, P. A., et al. 2012b, *ApJL*, **752**, L5
- Bouwens, R. J., Illingworth, G. D., Oesch, P. A., et al. 2012c, *ApJ*, **754**, 83
- Bouwens, R. J., Oesch, P. A., Illingworth, G. D., et al. 2012d, *ApJL*, **765**, L16
- Bradley, L. D., Trenti, M., Oesch, P. A., et al. 2012, *ApJ*, **760**, 108
- Brammer, G. B., van Dokkum, P. G., & Coppi, P. 2008, *ApJ*, **686**, 1503
- Brammer, G. B., van Dokkum, P. G., Illingworth, G. D., et al. 2013, *ApJL*, **765**, L2
- Bruzual, G., & Charlot, S. 2003, *MNRAS*, **344**, 1000
- Bunker, A. J., Caruana, J., Wilkins, S. M., et al. 2013, *MNRAS*, **430**, 3314
- Calzetti, D., Armus, L., Bohlin, R. C., et al. 2000, *ApJ*, **533**, 682
- Caruana, J., Bunker, A. J., Wilkins, S. M., et al. 2012, *MNRAS*, **427**, 3055
- Coe, D., Zitrin, A., Carrasco, M., et al. 2013, *ApJ*, **762**, 32
- Cucchiara, A., Levan, A. J., Fox, D. B., et al. 2011, *ApJ*, **736**, 7
- Ellis, R. S., McLure, R. J., Dunlop, J. S., et al. 2013, *ApJL*, **763**, L7
- Feldmann, R., Carollo, C. M., Porciani, C., et al. 2006, *MNRAS*, **372**, 565
- Ferguson, H. C., Dickinson, M., Giavalisco, M., et al. 2004, *ApJL*, **600**, L107
- Finkelstein, S. L., Papovich, C., Giavalisco, M., et al. 2010, *ApJ*, **719**, 1250
- Finkelstein, S. L., Papovich, C., Ryan, R. E., et al. 2012, *ApJ*, **758**, 93
- Finlator, K., Davé, R., & Özel, F. 2011, *ApJ*, **743**, 169
- Grazian, A., Castellano, M., Fontana, A., et al. 2012, *A&A*, **547**, A51
- Grogin, N. A., Kocevski, D. D., Faber, S. M., et al. 2011, *ApJS*, **197**, 35
- Illingworth, G. D., Magee, D., Oesch, P. A., et al. 2013, arXiv:1305.1931
- Jaacks, J., Choi, J.-H., Nagamine, K., Thompson, R., & Varghese, S. 2012, *MNRAS*, **420**, 1606
- Kistler, M. D., Yüksel, H., Beacom, J. F., Hopkins, A. M., & Wyithe, J. S. B. 2009, *ApJL*, **705**, L104
- Koekemoer, A. M., Ellis, R. S., McLure, R. J., et al. 2012, arXiv:1212.1448
- Koekemoer, A. M., Faber, S. M., Ferguson, H. C., et al. 2011, *ApJS*, **197**, 36
- Kuhlen, M., & Faucher-Giguère, C.-A. 2012, *MNRAS*, **423**, 862
- Labbe, I., González, V., Bouwens, R. J., et al. 2010, *ApJL*, **708**, L26
- Labbe, I., Oesch, P. A., Bouwens, R. J., et al. 2012, arXiv:1209.3037
- Lacey, C. G., Baugh, C. M., Frenk, C. S., & Benson, A. J. 2011, *MNRAS*, **412**, 1828
- Lorenzoni, S., Bunker, A. J., Wilkins, S. M., et al. 2013, *MNRAS*, **429**, 150
- Madau, P. 1995, *ApJ*, **441**, 18
- Madau, P., Pozzetti, L., & Dickinson, M. 1998, *ApJ*, **498**, 106
- McLure, R. J., Dunlop, J. S., Bowler, R. A. A., et al. 2013, *MNRAS*, **432**, 2696
- McLure, R. J., Dunlop, J. S., Cirasuolo, M., et al. 2010, *MNRAS*, **403**, 960
- Meurer, G. R., Heckman, T. M., & Calzetti, D. 1999, *ApJ*, **521**, 64
- Muñoz, J. A., & Loeb, A. 2008, *MNRAS*, **385**, 2175
- Oesch, P. A., Bouwens, R. J., Carollo, C. M., et al. 2010a, *ApJL*, **709**, L21
- Oesch, P. A., Bouwens, R. J., Illingworth, G. D., et al. 2012a, *ApJ*, **745**, 110
- Oesch, P. A., Bouwens, R. J., Illingworth, G. D., et al. 2012b, *ApJ*, **759**, 135
- Oesch, P. A., Carollo, C. M., Feldmann, R., et al. 2010b, *ApJL*, **714**, L47
- Oesch, P. A., Stiavelli, M., Carollo, C. M., et al. 2007, *ApJ*, **671**, 1212
- Oke, J. B., & Gunn, J. E. 1983, *ApJ*, **266**, 713
- Ono, Y., Ouchi, M., Curtis-Lake, E., et al. 2012, arXiv:1212.3869
- Papovich, C., Finkelstein, S. L., Ferguson, H. C., Lotz, J. M., & Giavalisco, M. 2011, *MNRAS*, **412**, 1123
- Peng, C. Y., Ho, L. C., Impey, C. D., & Rix, H. 2002, *AJ*, **124**, 266
- Pentericci, L., Fontana, A., Vanzella, E., et al. 2011, *ApJ*, **743**, 132
- Robertson, B. E. 2010, *ApJ*, **713**, 1266
- Robertson, B. E., & Ellis, R. S. 2012, *ApJ*, **744**, 95
- Salvaterra, R., Della Valle, M., Campana, S., et al. 2009, *Natur*, **461**, 1258
- Schenker, M. A., Robertson, B. E., Ellis, R. S., et al. 2013, *ApJ*, **768**, 196
- Schenker, M. A., Stark, D. P., Ellis, R. S., et al. 2012, *ApJ*, **744**, 179
- Smit, R., Bouwens, R. J., Franx, M., et al. 2012, *ApJ*, **756**, 14
- Stanway, E. R., McMahon, R. G., & Bunker, A. J. 2005, *MNRAS*, **359**, 1184
- Szalay, A. S., Connolly, A. J., & Szokoly, G. P. 1999, *AJ*, **117**, 68
- Tacchella, S., Trenti, M., & Carollo, C. M. 2013, *ApJL*, **768**, L37
- Tanvir, N. R., Fox, D. B., Levan, A. J., et al. 2009, *Natur*, **461**, 1254
- Trenti, M., Perna, R., Levesque, E. M., Shull, J. M., & Stocke, J. T. 2012, *ApJL*, **749**, L38
- Trenti, M., & Stiavelli, M. 2008, *ApJ*, **676**, 767
- Trenti, M., Stiavelli, M., Bouwens, R. J., et al. 2010, *ApJL*, **714**, L202
- Windhorst, R. A., Cohen, S. H., Hathi, N. P., et al. 2011, *ApJS*, **193**, 27
- Yan, H., Yan, L., Zamojski, M. A., et al. 2011, *ApJL*, **728**, L22
- Zheng, W., Postman, M., Zitrin, A., et al. 2012, *Natur*, **489**, 406